Mass balance and surface evolution of debris-covered Miage Glacier, 1990 - 2018

A.M. Stefaniak [a*], B.A. Robson [b], S.J. Cook [c,d], B. Clutterbuck [a], N.G. Midgley [a], J.C. Labadz [a]

[a] School of Animal, Rural and Environmental Sciences, Nottingham Trent University, Brackenhurst Campus, Southwell, Nottinghamshire, NG25 0QF, UK;

[b] Department of Geography, University of Bergen, Fosswinkelgate 6, 5007 Bergen, Norway;

[c] Geography and Environmental Science, School of Social Sciences, University of Dundee, Nethergate, Dundee, DD1 4HN, UK;

[d] UNESCO Centre for Water Law, Policy and Science, University of Dundee, Nethergate, Dundee, DD1 4HN, UK.

Email address: anne.stefaniak@ntu.ac.uk (A.M. Stefaniak)

Abstract

Many glaciers in high-mountain regions exhibit a debris cover that moderates their response to climatic change compared to clean-ice glaciers. Studies that integrate long-term observations of debris-covered glacier mass balance, velocity, surface debris evolution and geomorphological changes (such as ponds and ice cliffs) are relatively few. This study used satellite imagery, ground-based photogrammetry and bathymetry to assess such changes at Miage Glacier, Italian Alps, over a 28-year time period (1990 – 2018). Over this period, Miage Glacier experienced sustained negative mass balance (-0.86 ± 0.27 metres per year water equivalent [m w.e. a^{-1}])), a substantial reduction in surface velocity (-46%), and increased debris-cover extent (+8.5% of the total glacier area). Since 1990, supraglacial ponds and ice cliffs have become more prevalent; whilst only covering 1.2 – 1.5% of the glacier area, they account for up to 8 times the magnitude of the average glacier surface lowering. Subsequently, Miage Glacier has entered a phase of enhanced decay since 1990. Miage Glacier is expected to continue to slow and thin, although any further accelerations in its decay will depend upon whether or not the tributary glaciers become disconnected from the main trunk, which would reduce ice flow, promote stagnation, flatten the longitudinal profile, and facilitate more widespread development of supraglacial ponds and so enhance ablation.

Keywords: Mass balance, surface velocity, DEMs, remote sensing, Structure-from-Motion, bathymetric surveys.

1. Introduction

Most glaciers around the world are receding and/or thinning due to climatic change, but local topographic and dynamic factors can exert a strong influence on the rate of glacier change (IPCC, 2014; Zemp et al., 2015). The development of supraglacial debris cover is one such factor whereby ablation is reduced when a glacier-dependant critical thickness is exceeded, or promoted where debris is thin or diffuse (Benn et al., 2012; Fyffe et al., 2020; Mattson et al., 1993; Nicholson and Benn, 2006; Østrem, 1959; Scherler et al., 2011). Debris-covered glaciers respond differently to climatic variability in comparison to clean-ice glaciers and typically experience mass loss primarily by surface lowering more than through marginal recession (Hambrey et al., 2008). As such, debris-covered glaciers are often found at lower elevations than climatically equivalent clean-ice glaciers. During periods of negative mass balance, velocities reduce and melt-out of englacial debris increases (Kirkbride and Deline, 2013). Mass loss is focused on clean-ice areas often located upglacier of the terminus whereas the terminus itself become covered in a thick layer of debris (Anderson and Anderson, 2018; Benn et al., 2012; Benn and Lehmkuhl, 2000; Nakawo et al., 1999; Ragettli et al., 2016). This substantially alters the mass balance gradient compared to cleanice glaciers and promotes reduced driving stress and ice flow (Dehecq et al., 2019; Kääb, 2005; Quincey et al., 2009; Rowan et al., 2015). Further, supraglacial ponds and associated ice cliffs commonly develop on debris-covered glaciers, which locally enhance melt rates and have an important influence on glacier mass balance (Benn et al., 2012, 2001; Miles et al., 2018, 2016; Reid and Brock, 2014; Thompson et al., 2016; Watson et al., 2018, 2017a, 2017b). Consequently, integrated monitoring of glacier mass balance, supraglacial debris cover, and the presence of supraglacial ponds, lakes and ice cliffs is required to better understand debris-covered glacier response to climatic change (Anderson and Anderson, 2016; Gibson et al., 2017; Mölg et al., 2019; Rowan et al., 2015; Salerno et al., 2017).

This study is concerned with the mass balance and surface evolution of debris-covered Miage Glacier in the Mont Blanc massif, European Alps, over nearly three decades from 1990 to 2018. Miage Glacier is the largest debris-covered glacier located in the European Alps (Figure 1). The nearly-continuous debris cover, which developed after the Little Ice Age (LIA) termination, has had a profound impact on glacier evolution (Deline, 2005). Previous mass balance studies of the Mont Blanc region identified a strongly negative trend (-1.04 ± 0.23 metres per year water equivalent [m w.e. a^{-1}]) based on SPOT5 and Pleiades high-resolution Digital Elevation Models (DEMs) from 2003 to 2012 (Berthier et al., 2014). The rate of mass loss between 2003-2012 at Miage Glacier was found to be 19% lower (−0.84 ± 0.22 m w.e. a^{-1}.) than the Mont Blanc region average; this average value includes data from predominantly clean-ice glaciers, such as the Tre-la-téte, which experienced higher rates of mass loss (-1.34 ± 0.22 m w.e. a^{-1}; Berthier et al., 2014).

This study extends the census period of change from that of Thomson et al. (2000) who used cartographic and topographic surveys between 1913 and 1999 to illustrate a striking complexity of glacier evolution over space and time. Miage Glacier was found to have thickened overall between 1913 and 1957, especially evident on the terminal lobes equivalent to +0.14 m a^{-1} over the 44-year period. From 1957 to 1967, the glacier thinned by -0.38 m a^{-1}. However, changes across the glacier were heterogeneous with most loss over the valley trunk section of the glacier, but a 20 m elevation increase of the north terminal lobe. From 1967 to 1975, the terminal lobes then lost over 20 m in thickness, but widespread thickening of the valley tongue meant that, overall, the glacier thickened on average by +0.23 m a^{-1}. Further overall thickening of 1 m, or +0.04 m a^{-1}, occurred between 1975 and 1999, but this time with the thickening focussed on the terminal lobes, whereas decreasing thickness was observed further up-glacier. Diolaiuti et al. (2009) also identified a period of positive mass gain between 1975 and 1991, which was followed by a period of substantial mass loss between 1991 and 2003. During this period of heterogenous mass change, terminus retreat was limited in response to the thicker debris present on the terminal lobes typical of debris-covered glaciers (e.g. Hambrey et al. 2008). However, ice flux variability dominated compared to the influence of differential ablation. However, the presence of supraglacial ponds and ice cliffs were not reported within either of these previous studies.

The relatively recent development of supraglacial ponds and ice cliffs on Miage Glacier may have an important, yet under-appreciated, role in influencing the mass balance. The presence of glacial lakes at Miage Glacier has been documented (Diolaiuti et al., 2005; Tinti et al., 1999), but supraglacial ponds have received little detailed attention, with most studies focussing on the ice-marginal lake, Lake Miage, located on the southern margin as the glacier turns eastwards into Val Veny (Figure 1). Reid and Brock (2014) showed that ice cliffs comprised only 1.3% of the glacier surface area, but were responsible for ~7.4% of the ablation over 2010-2011. Given the wide range of glaciological and geomorphological research that has been undertaken at Miage Glacier, it is notable that there has been very little research on the nature and importance of supraglacial ponds and ice cliffs at this location in contrast to the volume of research undertaken on other debris-covered glaciers.

Debris-covered glacier response to climatic variability remains poorly understood because of the complex feedbacks between climate, mass balance, velocity, change in debris cover and surface features (ice cliffs and ponds) (e.g. Dehecq et al., 2019; Rowan et al., 2015). Studies that integrate observations of these elements over annual, decadal and centennial timescales, and across the full glacier extent can help to unpick some of these complexities. This study provides a detailed appraisal of the evolution and dynamics of the debris-covered Miage Glacier over a 28-year time period from 1990 to 2018. Our study overlaps with previous census periods for this glacier (Berthier et al., 2014; Diolaiuti et al., 2009; Thomson et al., 2000), enabling long-term evolution and dynamics to be assessed. Specifically, the objectives of this study are: (i) to quantify glacier surface change, (ii) to assess topographic and surface dynamic changes of Miage Glacier over multi-decadal and multi-annual time scales; (iii) to assess the role of supraglacial ponds and ice cliffs in the evolution of Miage Glacier; and (iv) to place our findings within the broader context of long-term observations at this glacier. Overall, this work provides an integrated assessment of the long-term evolution and feedbacks between mass balance, velocity, debris cover and surface features, which aids our understanding of debris-covered glacier response to climatic change in the world's high mountain regions.

2. Study site

Miage Glacier is located on the southwest flank of Mont Blanc (Monte Bianco) in the Italian Alps (45°45'N, 06°52'E; Figure 1). Miage Glacier is ~10 km long, with an altitudinal range from ~3000 m a.s.l. to ~1000 m a.s.l. and is fed by four tributary glaciers; Dome (DG), Bionnassay (BG), Mont Blanc (MB) and Tête Carrée (TC).

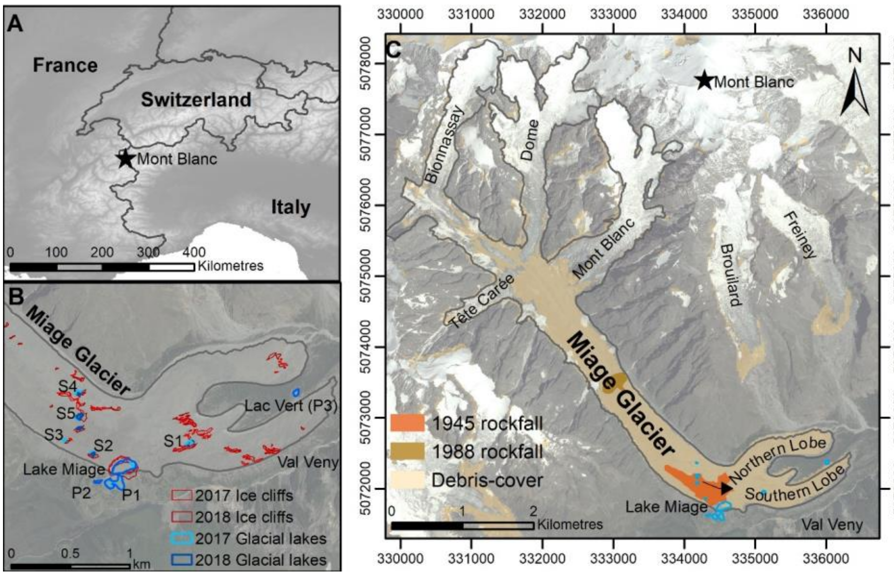

Figure 1: A: Location of Miage Glacier on the southwest flank of Mont Blanc. B: Locations of the glacial lakes including supraglacial ponds, and ice cliffs present during the surveys in summer 2017 and 2018. C: Miage Glacier is fed by 4 tributary glaciers and comprises a continuous debris cover from multiple rockfall events including those in 1945 and 1988.

Since the Little Ice Age (LIA; 1250 – 1850 CE), Miage Glacier has developed a continuous debris cover (Deline, 2005), and has been the subject of a wide range of glaciological studies including mass balance (Berthier et al., 2014; Smiraglia et al., 2000; Thomson et al., 2000), surface energy balance (Fyffe et al., 2014; Reid and Brock, 2010), near-surface meteorology (Brock et al., 2010; Shaw et al., 2016), hydrology (Fyffe et al., 2019), debris evolution (Deline, 2005), variable ablation patterns and debris redistribution (Fyffe et al., 2020), geomorphological evolution (Westoby et al., 2020), mass loss processes including ice cliffs (Diolaiuti et al., 2005; Reid and Brock, 2014), and the presence of glacial lakes and associated processes (Diolaiuti et al., 2006, 2005; Tinti et al., 1999).

Several types of glacial lake exist at Miage Glacier including an ice-marginal lake, proglacial lakes, and supraglacial ponds. Perhaps most notable due to its persistence is Lake Miage (Figure 1), a popular tourist attraction. Lake Miage has undergone repeat cycles of drainage and refilling with 16 documented drainage events in the twentieth century (Conforti et al., 2005). One of the largest drainage events occurred in 2004 over a period of 2 days (Masetti et al., 2010). Although the lake does not represent a significant glacial lake outburst flood (GLOF) hazard, the lake remains a large water store, with implications for runoff and local glacier mass loss including calving events and thermal undercutting (Diolaiuti et al., 2005).

3. Methods

A range of data sources were utilised for this study including satellite imagery for surface mapping, DEM production and surface velocity analysis, in addition to bathymetric and photogrammetry surveys conducted in 2017 and 2018. Satellite data ranged from coarse resolution (30 m) Landsat-derived surface velocity displacements from 1990/91 to 2017/18, to high-resolution (1.5 – 10 m) SPOT (1990, 2016 and 2018 data supplied by European Space Agency (ESA)), airborne LiDAR Digital Terrain Model (DTM; 2 m) (2008 data provided by the Autonomous Region Valle d'Aosta; (http://metadati.partout.it/metadata_documents/Specifiche_LIDAR.pdf), and Pleiades (2012 - 2014) (data supplied by ESA) DEMs (Table 1). DEM and surface velocity analyses were carried out in PCI Geomatica Orthoengine and open-source image correlation software CIAS (Heid and Kääb, 2012; Kääb and Vollmer, 2000).

Table 1: Data sets used within this study (SPOT and Pleiades data provided by ESA, 2008 LiDAR DEM from Valle d'Aosta). All datasets used the panchromatic band for DEM and SWIR for surface velocity extraction.

Date of acquisition (dd/mm/yr)	Sensor	Image Resolution (m)	Image Pairs	Data extracted
26/08/2018	SPOT-7	1.5	Stereo	DEM/Glacier mapping
13/07/2017	SPOT-7	1.5	-	Glacier mapping
12/10/2016	SPOT-7	1.5	Stereo	DEM/ Glacier mapping
26/08/2015	TerraItaly Orthophoto	0.2	-	Aid GCP collection
02/10/2014	Pleiades 1B	0.5	Stereo	DEM/ Glacier mapping
20/09/2013	Pleiades 1A	0.5	-	Glacier mapping
19/08/2012	Pleiades 1A	0.5	Stereo	DEM/ Glacier mapping
29/08/2009	GeoEye-1	0.5	-	Glacier mapping
20/08/2008	LiDAR – Valle d'Aosta	2.0	-	DEM
19/08/1990	SPOT-1	10.0	2 overlapping images	DEM/Glacier mapping
22/07/1990	SPOT-1	10.0		
20/09/1989	SPOT Ortho	10.0	-	Aid GCP collection
16/08/1990	Landsat5 TM	30.0	-	Surface Velocity
19/08/1991	Landsat5 TM	30.0		Surface Velocity
16/07/2008	Landsat5 TM	30.0	-	Surface Velocity

05/09/2009	Landsat5 TM	30.0		Surface Velocity
19/08/2017	Landsat8 OLI	30.0	-	Surface Velocity
23/09/2018	Landsat8 OLI	30.0		Surface Velocity

3.1. Glacier mapping

Manual digitisation of the glacier surface was undertaken using orthorectified SPOT (1990 and 2018) and GeoEye (2009) satellite imagery in ArcGIS (Table 1). Due to a lack of available imagery from 2008 to compliment the 2008 LiDAR DEM, an orthorectified GeoEye-1 image was used from 2009. The satellite images were orthorectified and pansharpened to aid identification of surface features. For each year surface features including glacier extent, debris cover, supraglacial ponds, and ice cliffs were manually digitised by one analyst and edited until no further edits were required (e.g. Watson et al., 2017a). Uncertainty was then assessed for each mapped component.

3.1.1. Glacier extent and terminal position

Identification of the glacier extent was aided by indicators of ice presence such as ice cliffs, exposed ice and distinct morphological changes to aid the mapping of the debris-covered ice. Mapping debris-covered glaciers is challenging due to the presence of debris obscuring the glacier surface, which increases the potential for error. Manual mapping is influenced by the image resolution and ambiguity in both identification and digitisation of surface features (Watson et al., 2017a). All images were registered to a common image (2015 orthophoto) allowing termini position, glacier and debris area and surface features to be quantified. For each glacier outline, manual digitisation was carried out three times for comparison and uncertainty was assessed via the standard deviation, ranging from 0.05 to 0.34 km^2 (Paul et al., 2013). The mean area for each year of the repeat digitisations varied by <5%. Assessment of the uncertainty for termini position was determined based on the square root of the input imagery resolution and registration error as in equation 1 (Hall et al., 2003; Silverio and Jaquet, 2005). Registration error compared to the 2015 orthophoto was determined to be <2 pixels ranging from 1 – 20 m for the 2018 to 1990 data. Uncertainty ranged from between 1.12 and 10.96 m respectively for the 2018 and 1990 termini positions.

$$Uncertainty = \sqrt{[(pixel\ resolution\ image1)^2 + (pixel\ resolution\ image2)^2]} + registration\ error$$

[Equation 1]

3.1.2. Debris cover

Debris cover was mapped within the glacier extent aided by a simple maximum likelihood classification in ArcGIS using debris and snow/ice classes with training data of 10 spectral samples for each image, and manually edited. Due to limited ground truth data other than field observations to confirm regions of debris cover, uncertainty was applied at an upper boundary of ±5% in accordance with previous studies (e.g. Mölg et al., 2018; Paul et al., 2017, 2013).

3.1.3. Supraglacial ponds

Supraglacial ponds were manually mapped from 1990 SPOT, 2009 GeoEye-1 and 2018 SPOT-7 images in addition to 2012 – 2014 Pleiades images, 2015 TerraItaly orthophoto and 2016 - 2017 SPOT imagery (Table 1). With the exception of the 1990 SPOT data, mapping was aided by a Normalized Difference Water Index (NDWI) band ratio utilising the near infrared (NIR) and visible green bands to identify water on the glacier surface (McFeeters, 1996). Assessment of the 2017 and 2018 imagery was also informed by field observations. Operator bias was assessed on five ponds randomly selected from the study area that were digitised independently three times as manual digitisation is likely to be a substantial source of uncertainty. The percentage variability for repeatability was <10% with a standard deviation range of 3 to 78 m^2. Total uncertainty for pond delineations was calculated as equal to the coefficient of variation for operator bias as adapted from Steiner et al. (2019) and ranged from 6.5 to 10.4%.

3.1.4. Ice cliffs

Ice cliffs were manually digitised from the 2009 GeoEye-1 and 1990 and 2018 SPOT imagery, in addition to 2012 – 2014 Pleiades images, 2015 TerraItaly Orthophoto and 2016 – 2017 SPOT imagery (Table 1). Ice cliffs were defined as exposed ice inclusive of both clean and dirty regions which were visually assessed. An image segmentation of the 1990 imagery was used to aid delineation of ice cliffs due to lower resolution and reduced contrast. Associations with supraglacial ponds and increased slope angles and aspect derived from the DEMs, aided identification of ice cliffs in comparison to the surrounding terrain. Uncertainty was assessed on a random sample of five ice cliffs that were selected from each of the images and digitised three times to assess operator error. The percentage variability for repeatability was <8% with standard deviations ranging from 20.6 to 185 m^2; lower variability was observed with the higher resolution data and was highest for the lower resolution data, which indicates a higher degree of uncertainty for the 1990 mapping. The coefficient of variation ranged from 3.13 to 6.5%.

3.2. Digital Elevation Model (DEM) extraction

The data sets used for DEM production were acquired during the ablation season to provide input images with little or no snow cover at similar dates for each year (ideally July to September). The number of useable data sets was limited by cloud cover and appropriate viewing-angles required for elevation extraction. Where possible, contemporaneous tri-stereo data were used for higher accuracy DEMs to be produced due to the inclusion of nadir imagery.

All DEMs (1990 - 2018) were produced based on automatic stereo-correlation using the normalised cross correlation (NCC) algorithm. The images were aligned based on the Rational Polynomial Coefficient (RPC) models and geolocation was improved by use of additional Ground Control Points (GCPs) obtained from high-resolution 2015 orthoimagery (0.2 m). Tie-points were then identified in each image pair (Table 2). GCPs based on ortho-corrected imagery from 1989 with the same resolution were used to improve the georeferencing. Tie-points were then automatically selected in corresponding image pairs. GCPs and tie-points maintained low residuals, <5.5 pixels equating to <16 m for the 1990 DEM, and <3 m for all other DEMs. All automatically assigned GCPs and tie-points were manually checked to remove any erroneous points. The number of GCPs varied depending on the ability to accurately identify matching locations (Table 2). As such, increased numbers of tie-points were used to aid point matching for elevation extraction.

Table 2: Summary of the GCPs and tie-points used to enhance the alignment of the imagery prior to DEM production.

DEM	Number of GCPs	Residuals X, Y (Pixels)	Number of tie-points	Residuals X, Y (Pixels)
1990	90	0.79, 0.34	150	1.56, 0.23
2012	2	1.53, 2.10	96	0.12, 0.03
2014	2	2.18, 5.41	64	0.22, 0.06
2016	36	0.39, 0.64	48	0.14, 0.04
2018	16	0.54, 1.51	40	0.10, 0.03

During the DEM production, smoothing was set to medium with a Wallis filter in PCI Geomatica Orthoengine to improve image contrast in areas of shadow and reduce noise in the resulting models (Baltsavias et al., 2007). DEMs were produced at extra high detail within mountainous terrain to enable extraction of finer details including ice cliffs to produce a geocoded DEM output at twice the resolution of the input data and range from a 20 m 1990 DEM, to two 1 m resolution Pleiades datasets from 2012 and 2014. SPOT6 and 7 data are now available in 12-bit pixel depth and are therefore comparable to Pleiades data providing higher radiometric resolution and improved contrast over snow/ice, which reduces the signal saturation. However, as Miage Glacier is mainly debris-covered, this improvement for mapping is less important in this study with the exception of the higher accumulation zones and tributary glaciers.

The DEMs were cleaned, edited and assessed based on the correlation scores. Correlation coefficient scores range from 0 indicating a total mismatch, to 1 indicating a perfect match for each image pixel (Cheng, 2015). Pixels with poor correlation resulting from poor matches (<0.5) and identifiable interpolation errors outside of the glacier extent were removed to aid co-registration. A total of five DEMs were generated from satellite images to determine temporal change in surface elevation and geodetic mass balance.

3.3. DEM differencing

In order to assess change over time, DEM differencing was carried out based on the co-registration method developed by Nuth and Kääb (2011). This method provides a workflow for DEM co-registration and bias correction via minimising root mean square residuals of the elevation biases over stable terrain as previously detailed in Robson et al. (2018). Unstable areas within the imagery including all glaciated areas, were masked out to aid co-registration on stable terrain. Each pair of DEMs (e.g. 1990 and 2008) were co-registered separately. Filtering and editing was undertaken with pixels with surface changes exceeding three times the standard deviation of the stable terrain elevation bias removed and spline and polynomial interpolations used to fill the gaps following the approaches by Bolch et al. (2011) and Gardelle et al. (2013).

Table 3: DEM co-registration shifts and DEM differencing uncertainty. The mean deviation, standard deviation and uncertainty are based on the co-registered DEM pairs. Statistics are based on stable (non-

glacier) terrain. DEM differencing uncertainty represents the sum of standard errors for each 100 m elevation band.

DEMs	X (m)	Y (m)	Z (m)	Mean deviation (m)	Standard deviation (m)	DEM differencing uncertainty (m)
1990-2018	-5.1	0.7	-2.1	-0.2	24.6	0.22
1990-2008	-2.8	-3.8	-2.6	1.0	13.5	0.27
2008-2018	1.0	3.7	-0.6	-0.7	6.4	0.12
2012-2018	1.8	2.5	0.5	0.6	5.4	0.10
2012-2014	1.6	-4.4	-0.2	0.7	4.3	0.10
2014-2016	-3.2	1.9	-0.4	-1.0	4.8	0.09
2016-2018	3.2	2.9	0.5	0.5	5.9	0.20

Surface elevation change was calculated based on the mean change over each time period of DEM differencing for areas delineated by glacier extents relevant to the start of that time period. The geodetic mass balance was then determined based on an assumed ice density of 850 ± 60 kg m^{-3} (Huss, 2013). Emergence velocity was not calculated for this study following commonly used methods for glacier-wide geodetic mass balance calculations .(e.g. Berthier et al., 2016; Gardelle et al., 2013; Paul et al., 2007; Pellicciotti et al., 2015; Thompson et al., 2016; Thomson et al., 2000). Furthermore, ice thickness data required for the calculation would be subject to further uncertainty.

In order to determine the uncertainty for glacier surface elevation change and geodetic mass balance, the approach outlined by Gardelle et al. (2013) as described by Falaschi et al. (2019) was used. This method accounts for the uncertainties relating to (i) the volume to mass conversion (Ep), (ii) the uncertainty related to glacier area digitisation (Ea), and (iii) the glacier volume change uncertainty ($E\Delta v$). A density of 860 ± 60 kg m^{-3} was used to convert the ice volume to a mass (Ep), following (Huss, 2013) and a glacier area uncertainty of 5% based on the value from repeat digitisations (Ea). The total volume change uncertainty ($E\Delta v$) was determined over 50 m elevation bands ($E\Delta vi$) based on the standard error (SE). The standard error (SET) considers the standard deviation of elevation changes over stable terrain (equation 2), the number of pixels in the DEM difference in that elevation band (equation 3), and the degree of spatial autocorrelation, which, based on Bolch et al. (2017), was taken to be 20 times the pixel size (King et al., 2017). The volume change uncertainty per elevation band ($E\Delta vi$) was then summed-up over the entire glacier (equation 4). Finally, *Ep*, *Ea* and $E\Delta v$ were combined in a root mean square sum (equation 5). The surface elevation change uncertainty ranged from ±0.01 to ±0.13 m, and the geodetic mass balance uncertainties ranged from ±0.09 to ±0.27 m w.e. a^{-1} (Table 3).

$$E\Delta h = \frac{\sigma stable}{\sqrt{N}} \qquad \text{[Equation 2]}$$

$$N = \frac{Ntot \times PS}{2d} \qquad \text{[Equation 3]}$$

$$E\Delta vi = \sum_{i}^{n} E\Delta hi * Ai \qquad \text{[Equation 4]}$$

$$E\Delta tot = \sqrt{E^2\Delta v + E^2 p + E^2 a} \qquad \text{[Equation 5]}$$

3.3.1. Ice cliff and pond contributions to thinning rates

Ice cliff and pond contributions to thinning rates were extracted based on the delineated polygons and relevant DEM of difference (e.g. polygons of ice cliffs present in 2012, 2013 and 2014 were merged and extracted from the 2012 – 2014 DEM differencing). This approach aims to capture the evolution of the features throughout the DEM differencing period. A similar approach was used by Thompson et al. (2016). This approach likely represents an underestimation of the contributions as distal ablation is not accounted for; however, many of the supraglacial ponds neighbour ice cliffs and by including any distal ablation would incorporate this contribution twice. Furthermore, assessment of the contribution of supraglacial ponds is based on the surface water level and does not consider subaqueous ablation. Uncertainty of these contributions is estimated based on the approach by Steiner et al. (2019) combining the operator bias coefficient of variation and DEM uncertainty; this equates to 5% for ice cliffs and 7% for supraglacial ponds.

3.4. Surface velocity

Surface velocity was measured using a feature-tracking approach. Pairs of Short Wave Infrared (SWIR) band Landsat5 Thematic Mapper (TM) and 8 Operational Land Imager (OLI) imagery from 1990/1991, 2008/2009 and 2017/2018 were used to determine annual glacier velocities (Table 1) from the same orbit (row/path) to aid surface velocity tracking. Features on the surface were matched using a NCC-O cross-correlation of orientation images using open-source software CIAS (Kääb and Vollmer, 2000). Orientation images were used to reduce the influence of scene illumination by using gradients between neighbouring pixel values instead of raw digital numbers where variations in scene illumination and presence/absence of shadow varied (Robson et al., 2018). Surface features were tracked in CIAS providing displacement vectors. Reference block size and search size were set in relation to the input image resolution while the search size was set to twice the expected surface velocity. As the input images all had the same resolution, the block, search and output resolution values were set to 15, 20 and 30 respectively.

Displacement vectors were filtered by initially removing those with a signal to noise ratio (SnR) <0.5 and points associated with cloud or shadow. They were then filtered by direction and magnitude, removing any apparent erroneous points. A 3x3 focal statistics filter was used to remove displacement vectors, which varied more than 20% in direction or magnitude to the surrounding mean values (Robson et al., 2018). Displacement vectors were then converted into surface velocity per year.

GNSS positions of 6 boulders were recorded during field visits in 2017 and 2018 using a Trimble Geo7x GNSS and post-processed using RINEX data from the Morgex base station <15 km from Miage Glacier. The mean accuracy of position data was ±0.03 m, enabling comparison of surface velocity rates around Lake Miage. Analysis of boulder movement shows an average of 12 m a^{-1} complementing the results from the 2017 - 2018 surface velocity data.

Surface velocity accuracy was determined by measuring displacements over stable terrain based on 87 random points <500 m from Miage Glacier termini. The points were situated along stable terrain with a gentle slope, free from shadow and snow/cloud were identified from satellite imagery and fieldwork. The accuracy associated with the surface velocity feature tracking is stated in Table 4.

Table 4: Accuracy assessment of the surface velocity feature tracking .

Surface velocity data set	Standard Deviation (m a^{-1})	Mean (m a^{-1})
1990 – 1991 Landsat 5	5.29	9.18
2008 – 2009 Landsat 5	2.25	5.71
2017 – 2018 Landsat 8	4.82	6.58

3.5. Bathymetry surveys

Bathymetric surveys of the ice-marginal lake (Lake Miage), three proglacial lakes (P1 - P3) and five supraglacial ponds (S1 – S5, Figure 1) were undertaken in July 2017 and July 2018. A Seafloor Systems

Hydrone remote control bathymetric survey boat with an Ohmex SonarMite BTX v4/5 echo sounder, with a reported accuracy of ±0.0025 m, was used wherever ponds with depths were sufficient to accommodate the survey boat. Although smaller ponds were present (<10 were observed), they were too small to survey with the boat.

The level of the water edge was surveyed with the Trimble Geo7x GNSS where accessible and post-processed. Lake and pond extents were accurate to a mean XYZ positional accuracy of 0.06 m; however, due to the obscured view of the sky by the ice cliffs, some points during the bathymetric survey recorded a lower accuracy but were not excluded from the datasets to ensure a complete coverage. All points recorded an accuracy of <1.5 m with the exception of the S4 2017 survey which recorded some points with a maximum accuracy of 4.8 m.

The bathymetric survey boat collected 2-3 depth measurements per second, travelling at an average speed of 1.5 m s^{-1}. Survey point summary and errors are provided in Table 5. For each survey, water level points were taken with the Trimble GNSS and included in the bathymetric interpolation to improve area and volume calculations using ArcGIS. It was not possible to collect water level/edge points where ice cliffs were present, so SPOT imagery and the photogrammetric models were used to delineate the extent of ponds along the ice cliffs. Although previous studies have adopted a natural neighbour approach (e.g. Thompson et al., 2016; Watson et al., 2018), three interpolation methods were tested and the accuracy of predictions assessed using an RMSE. Out of the natural neighbour, IDW and spline algorithms tested, IDW produced the lowest estimates whilst enabling preservation of data measurements and was therefore adopted in this study. A suitable output resolution was assessed based on the mean distance between points.

Table 5: Number of depth measurements, average XY GNSS accuracy and RMSE for the IDW interpolations for the bathymetric maps.

Lake		Number of depth measurements	Average XY GNSS Accuracy (m)	Average interpolation standard error (RMSE)
Lake Miage – Ice-marginal	2017	8149	0.022	0.390
lake	2018	4007	0.367	0.344
Proglacial lake 1 – P1	2017	5783	0.024	0.108
	2018	6052	0.191	0.113
Proglacial lake 2 – P2	2017	1224	0.040	0.046

	2018	1723	0.024	0.101
Lac Vert – P3	2017	4025	0.461	0.065
	2018	1986	0.364	0.069
Supraglacial pond 1 – S1	2017	5059	0.026	0.438
	2018	1735	0.048	0.134
Supraglacial pond 2 – S2	2017	3256	0.023	0.764
	2018	1217	0.027	0.853
Supraglacial pond 3 – S3	2017	2032	0.020	0.129
	2018	-	-	-
Supraglacial pond 4 – S4	2017	2420	0.280	0.030
	2018	850	0.019	0.076
Supraglacial pond 5 – S5	2017	-	-	-
	2018	1879	0.021	0.488

3.6. Photogrammetry surveys

Ground-based photogrammetry surveys were limited to supraglacial ponds with adjacent ice cliffs and undertaken in clear weather conditions. Ice cliffs were also observed elsewhere on the glacier but did not have associated supraglacial ponds and were not surveyed.

Each ice cliff survey typically took <2 hours, with between 126 to 415 images dependent on cliff size and extent of undulating topography. Images were taken with a Sony Alpha 7R digital camera with a fixed focal length lens (35 mm) and 42-megapixel sensor. A range of ground-based camera locations with oblique angles were used to provide good coverage of the ice cliff, water edge and surrounding areas where identifiable A3 paper sized fluorescent yellow and orange ground-based control points (GCPs) were placed with a central black marker. GCPs were distributed at various heights and locations to encompass the survey area and the locations of the targets were recorded with the Trimble Geo7x GNSS. Positional data was post-processed with a mean accuracy of ±0.03 m.

Photos of the ice cliffs were processed using Structure from Motion (SfM) workflows in Agisoft Photoscan to create 3D representations of the ice cliffs as point clouds (e.g. Westoby et al., 2012). Processing followed the in-built workflows in Agisoft prior to export. Photos were aligned and those with a low-quality value (<0.7) were removed from the model based on quality estimations and visual checks. Once a sparse point cloud was processed, outliers from the area of interest were removed, retaining the maximum number of points with an acceptable error (<1 pixel). A dense point cloud was processed with 'high quality' settings. Georeferencing accuracy was <0.08 m and 3D GCP placement uncertainty was typically <0.04 m (Table 6).

During processing some areas could not be resolved due to sparse imagery coverage or unfavourable slope angles including channels transporting meltwater to supraglacial ponds from adjacent ice cliffs. A total of six GCPs were used for each model to reduce vertical errors (Tonkin and Midgley, 2016). Control and check points were used to assess the resulting models and are reported in Table 6.

The models were exported as 3D point clouds along with orthophotos and DEMs for further analysis in ArcGIS and CloudCompare. The models were analysed to calculate ice cliff area (calculated as the exposed surface), maximum ice cliff height, slope and aspect. Slope and aspect were calculated using the dip direction and angle tools within CloudCompare.

Table 6: Errors of the photogrammetric ice cliff models during processing and summary of GCPs, check points and accuracy.

Lake or pond		Resolution /pix	Georeferencing XYZ uncertainty (m)	Mean point density (per m^2)	No. Control GCPs	RMSE – Control (m)	No. check points	Accuracy – Check (m)
S1	2017	3.58 mm	0.028	5.9×10^4	6	0.04	3	0.05
	2018	2.09 mm	0.028	4.0×10^4	6	0.06	7	0.06
S2	2017	5.28 mm	0.026	2.2×10^4	6	0.02	13	0.05
	2018	3.69 mm	0.034	3.7×10^4	6	0.03	11	0.06
S3	2017	1.84 mm	0.026	1.7×10^5	6	0.02	12	0.05
	2018	1.47 mm	0.032	1.5×10^4	6	0.03	8	0.06
S4	2017	3.31 mm	0.027	6.6×10^4	6	0.02	3	0.08
	2018	2.59 mm	0.026	1.1×10^5	6	0.07	7	0.07
S5	2017	-	-	-	-	-	-	-
	2018	3.50 mm	0.032	4.5×10^4	6	0.07	7	0.08
Miage	2017	12.1 mm	0.030	3.4×10^3	6	0.02	17	0.05
	2018	8.9 mm	0.028	6.6×10^3	6	0.03	20	0.06

The SfM model point clouds were aligned based on identifiable boulders to account for displacements between the two surveys in 2017 and 2018 except for Lake Miage which originates on stable ground at the western margin. Once co-registered, ice cliff change was quantified using the Multiscale Model to Model Cloud Comparison (M3C2) cloud-to-cloud differencing method in CloudCompare as this method has been shown to be effective for determining change in river canyon and glacial environments based on the methods described by Lague et al. (2013), Westoby et al. (2016), Midgley and Tonkin (2017), Watson et al. (2017b) and Bash et al. (2018).

Distance calculations were clipped to the ice cliff faces and retreat rates calculated for the survey period between 2017 and 2018. Ice cliffs at Lake Miage were separated into north and south-facing sections to improve point detection with the M3C2 algorithm. Total errors were calculated for each ice cliff model using the georeferencing errors and displacement error between the two corresponding surveys.

4. Results

4.1. Glacier surface change

Miage Glacier underwent substantial surface change between 1990 and 2018 (Table 7; Figure 2). The glacier area decreased by 11 ± 3% between 1990 and 2018 with ~50 ± 10.96 m recession in termini extent. The reduction in glacier area is noted in the higher elevation accumulation zone and where tributary glaciers feed the Miage Glacier valley tongue (Figure 2). Debris cover increased between 1990 and 2018 by ~8.5%, with higher elevations and tributary glaciers becoming noticeably dirtier. Supraglacial ponds substantially increased in number between 1990 to 2018. No supraglacial ponds were observed in 1990 but they covered 6,047 m^2 by 2018, although the ice-marginal Lake Miage is evident since 1990. Because of its large size, trends in glacial lake area were driven largely by changes of Lake Miage. Alongside the development of lakes and ponds was an increase in ice cliff area from 16,772 m^2 to 47,616 m^2 (+184%).

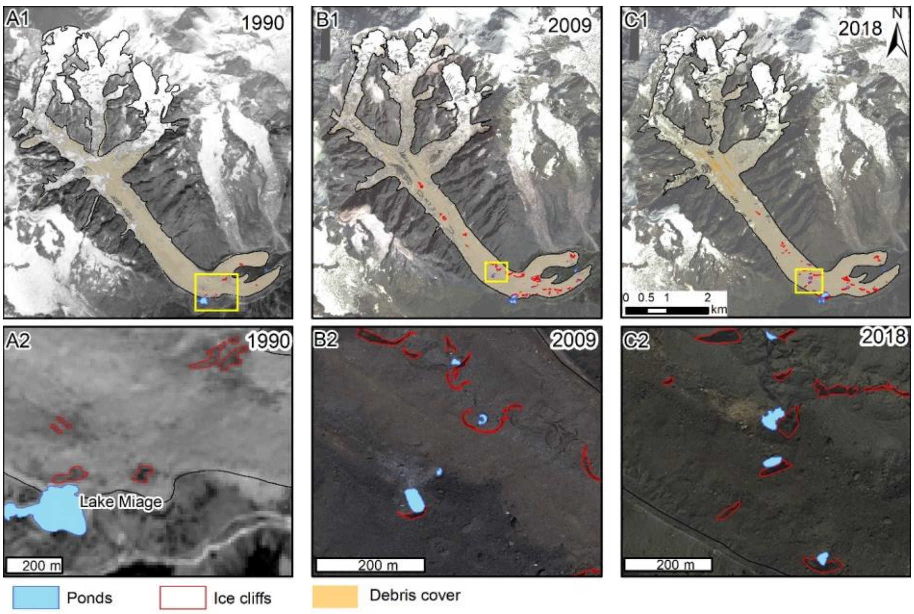

Figure 2: Glacier surface change from A1-2: 1990, B1-2: 2009 and C1-2: 2018 highlighting the increasing presence of the ice-marginal Lake Miage, supraglacial ponds and ice cliffs. Yellow boxes in top row refer to

the area shown in the bottom row figure highlighting regions with the high concentrations of supraglacial ponds and ice cliffs. Background data consists of A: 1990 SPOT1 greyscale imagery, B: 2009 GeoEye RGB imagery, C: 2018 SPOT7 RGB imagery.

Table 7: Summary of main surface features on Miage Glacier in 1990, 2009 and 2018 and percentage of total glacier area in parentheses. *Glacial lakes includes the proglacial lakes ice-marginal Lake Miage and supraglacial ponds.

Year	Glacier area (km^2)	Debris cover area (km^2)	Water storage area of glacial lakes* (m^2)	Supraglacial ponds (m^2)	Ice cliffs (m^2)
1990	10.5 ± 0.34	4.5 ± 0.23 (43%)	27897 ± 2790 (0.27%)	0	16772 ± 1342 (0.16%)
2009	9.6 ± 0.05	4.8 ± 0.24 (50%)	27731 ± 2773 (0.29%)	3407 ± 341 (0.04%)	36502 ± 2920 (0.38%)
2018	9.3 ± 0.05	4.9 ± 0.25 (53%)	34468 ± 3447 (0.37%)	6047 ± 605 (0.07%)	47616 ± 3809 (0.51%)

4.2. Surface elevation change and geodetic mass balance 1990 - 2018

Between 1990 and 2018, Miage Glacier experienced substantial downwasting of -1.01 ± 0.09 m a^{-1} on average; however, thinning rates have slowed from -1.07 ± 0.16 m a^{-1} between 1990 and 2008, to -0.85 ± 0.06 m a^{-1} between 2008 and 2018 (Table 8).

Table 8: Vertical surface elevation change and geodetic mass balance of Miage Glacier from 1990 to 2018 based on DEM differencing. Standard errors for elevation change and uncertainty values for geodetic mass balance provided.

Date	Surface elevation change (m a^{-1})	Mean geodetic mass balance (m w.e. a^{-1})	Debris-covered region surface elevation change (m a^{-1})
1990 - 2018	-1.01 ± 0.09	-0.86 ± 0.27	-1.25 ± 0.09
1990 - 2008	-1.07 ± 0.13	-0.88 ± 0.22	-1.17 ± 0.13
2008 - 2018	-0.85 ± 0.01	-0.67 ± 0.12	-1.30 ± 0.01
2012 – 2018	-0.62 ± 0.02	-0.53 ± 0.10	-1.82 ± 0.02
2012 – 2014	-0.51 ± 0.10	-0.35 ± 0.17	-1.36 ± 0.10
2014 – 2016	-0.45 ± 0.03	-0.30 ± 0.09	-0.92 ± 0.03
2016 – 2018	-0.85 ± 0.10	-0.64 ± 0.20	-1.21 ± 0.10

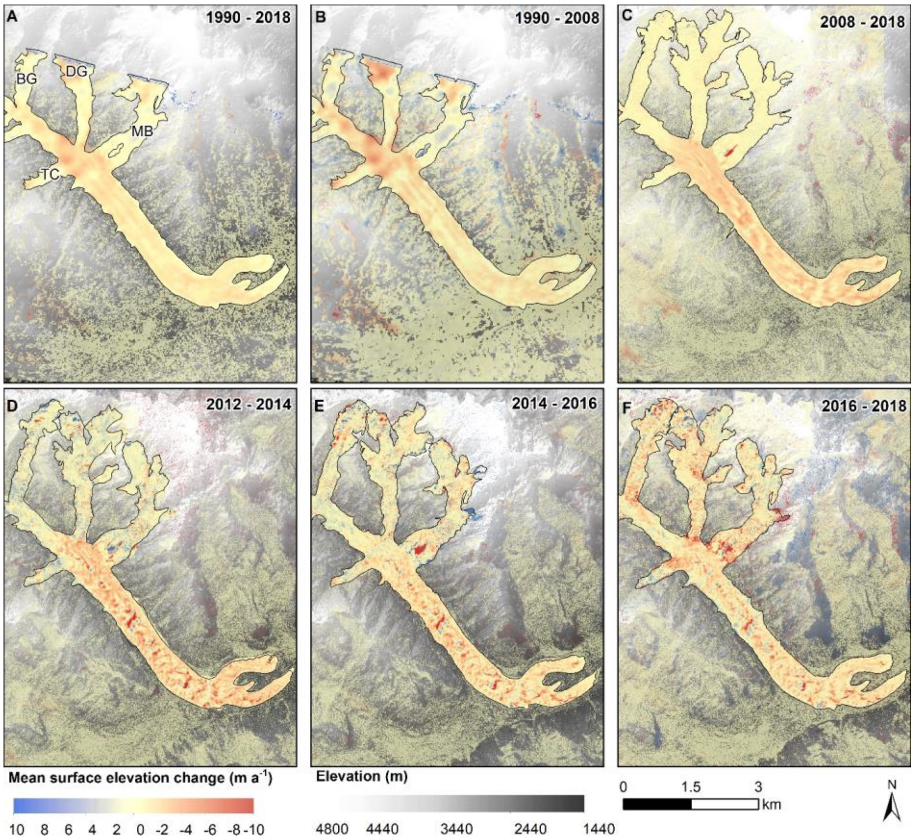

Figure 3: Mean annual surface elevation change in metres with a hillshaded elevation model as background. A: 1990 – 2018, B: 1990 – 2008, C: 2008 – 2018, D: 2012 – 2014, E: 2014 – 2016, F: 2016 - 2018. Note uncertainty associated with the nunatak at the base of Mont Blanc Glacier due to shadow in input data.

High thinning rates were evident at the base of Tête Carrée Glacier (TC) and Bionnassay Glacier (BG) where debris cover has expanded over the period (Figure 3). In comparison, the debris-covered valley tongue has undergone sustained downwasting over the full period, but thinning rates are reduced on the terminal lobes. From 1990 - 2018, the debris-covered region experienced mean annual downwasting of -1.25 ± 0.09 m a^{-1}; in comparison, the terminal lobes underwent thinning rates of -0.94 ± 0.09 m a^{-1}. The tributary glaciers present the largest increases in surface elevation associated with snow accumulation and ice dynamics at higher elevations (Figure 3).

Pleiades and SPOT6/7 DEM differencing from 2012 to 2018 enables recent change to be explored at higher spatial and temporal resolutions (Figure 3). Table 8 indicates that the rate of thinning has increased over the period 2012 to 2018 from -0.51 ± 0.04 m a^{-1} between 2012 to 2014, to -0.85 ± 0.10 m a^{-1} from 2016 to 2018, with an average surface elevation change of -0.62 ± 0.02 m a^{-1} over the period 2012 – 2018, yet these rates are lower than the 2008 – 2018 period indicating reduced mass loss in the last decade.

Heterogeneous elevation change is evident across the glacier surface with enhanced thinning at the base of Mont Blanc Glacier (MB) associated with a physical detachment and icefall events resulting in a visibly larger nunatak area. The nunatak at the base of Mont Blanc Glacier was often in shadow in the input data and likely to be responsible for the uncertainty associated with opposing trends in the Figure 3.

4.3. Surface velocity change 1990 -2018

Over the observation period the mean surface velocity of the glacier decreased by 46% from 35 ± 0.05 m a^{-1} in 1990/91 to 16 ± 0.05 m a^{-1} in 2017/18, (Figure 4). The ice in the terminal lobes have undergone a strong reduction in mean surface velocity over the same period from 20 ± 0.23 m a^{-1} to 6 ± 0.11 m a^{-1}, a surface velocity reduction of 70%. By 2018, central parts of the northern and southern lobes are nearly stagnant at <3 m a^{-1}.

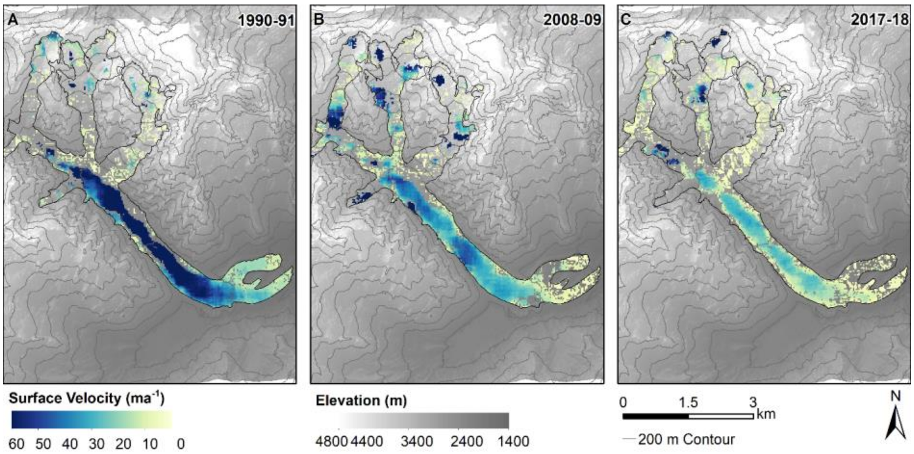

Figure 4: Landsat-derived surface velocity. A: 1990 – 1991, B: 2008 – 2009, C: 2017 - 2018. Contours shown at 200 m intervals.

4.4. Analysis of supraglacial ponds and ice cliffs

Surface elevation change patterns from 2012 to 2018 show specific regions with higher thinning rates (Figure 3) that are coincident with supraglacial ponds and ice cliffs (Figure 5). Areas of positive elevation change are evident attributed to advection of hummocky topography, pond water level change or debris redistribution. For each DEM, the associated surface change in areas with mapped supraglacial ponds and ice cliffs was extracted (Table 9). All ponds and ice cliffs present in the satellite imagery from 2012, 2013 and 2014 were merged and extracted from the 2012 – 2014 DEM differencing, and repeated for the 2014 -2016 and 2016 – 2018 periods.

For the periods 2012 – 2014 and 2014 – 2016 comparable rates of surface lowering (-3.77 ± 0.10 m a^{-1} and -3.79 ± 0.20 m a^{-1} respectively) were determined at ice cliff locations. However, in the latter period of assessment (2016 – 2018) surface lowering had reduced to -3.48 ± 0.25 m a^{-1} when ice cliffs presented a lower percentage of the debris-covered area during this time (Table 9).

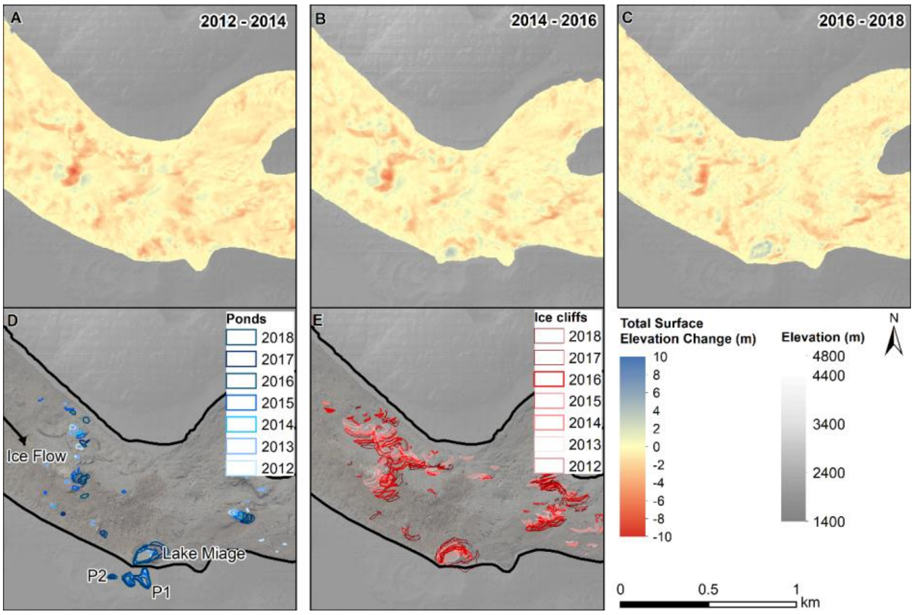

Figure 5: A: Total surface elevation change from 2012 – 2014, B: Surface change from 2014 - 2016, and C: Surface change from 2016 – 2018, and D: Locations of supraglacial ponds from 2012 - 2018 and E: Locations of ice cliffs from 2012 - 2018.

Table 9: Variations in geodetic mass balance associated with supraglacial ponds and ice cliffs, and density as a percentage of the debris-covered area from RGI6.0 analysis. Magnitudes of pond and ice cliff surface lowering are also presented. Uncertainty was calculated at 5% for ice cliffs and 7% for supraglacial ponds.

Year	Ice cliff elevation change (m a^{-1})	Ice cliff density as % of glacier area	Magnitude of average surface lowering	Pond elevation change (m a^{-1})	Pond density as % of glacier area	Magnitude of average surface lowering
2012 - 2014	-3.77	1.07	-7.39	-4.11	0.15	8.05
2014 - 2016	-3.79	1.32	8.42	-1.78	0.21	3.96
2016 - 2018	-3.48	0.99	4.09	-4.55	0.27	5.35

Although supraglacial ponds and ice cliffs exhibit up to 8 times the average glacier surface lowering, the quantification is complex since ice cliffs also backwaste and energy dissipates beyond the pond outlines which is not accounted for, thus the figures in Table 9 represent minimum contributions. Therefore, to further explore the influence of supraglacial ponds and ice cliffs at Miage Glacier, bathymetric and photogrammetry surveys undertaken in 2017 and 2018 examined the evolution of five supraglacial ponds and Lake Miage, and their associated ice cliffs (Figure 6). The supraglacial ponds (S1 – S5) held a volume of 13,595 m^3 in 2017, which increased to ~20,000 m^3 by 2018, accounting for 8% of the total water volume stored at the Miage Glacier surface (Table 10).

Table 10: Area, depth, lake levels and volume of lakes and ponds surveyed July 2017 and 2018. *S5 area in 2017 estimated from satellite imagery. Uncertainties calculated from RMSE.

	Year	Area (m^2)	Max. depth (m)	Water level elevation (m)	Volume (m^3)
Lake Miage ice marginal	2017	11,931	36.94 ± 0.39	2007.60	119,968 ± 0.06
	2018	16,028	30.56 ± 0.34	2009.81	170,354 ± 0.06
Supraglacial pond 1 (S1)	2017	1,495	13.30 ± 0.42	1964.30	7,600 ± 0.02
	2018	1,989	16.68 ± 0.10	1962.50	11,426 ± 0.01
Supraglacial pond 2 (S2)	2017	569	26.73 ±0.76	2030.20	3,112 ± 0.00
	2018	500	16.80 ± 0.85	2026.65	2,384 ± 0.00
Supraglacial pond 3 (S3)	2017	232	4.18 ± 0.13	2049.20	298 ± 0.02
	2018	-	-	-	-
Supraglacial pond 4 (S4)	2017	698	14.05 ± 0.03	2054.60	2,585 ± 0.00
	2018	207	5.27 ± 0.08	2048.40	323 ± 0.00
Supraglacial pond 5 (S5)	2017	1,464*	-	-	-
	2018	1,488	21.61 ± 0.49	2044.48	5,781 ± 0.12

The supraglacial ponds and Lake Miage show fluctuations in volume and area between the two surveys with the Lake Miage, S1 (Figure 6, A2-A3), and S5 experiencing volume increases (Figure 6, E2–E3), whilst S2 (Figure 6, B2-B3), S3 (Figure 6, C2-C3) and S4 underwent volume decreases (Figure 6, D2-D3). S3 drained completely between 2017 and 2018, which appears to be associated with a crevasse observed in this location in 2018 where the pond previously occupied in 2017 (Table 10). The supraglacial ponds and Lake Miage surveyed in 2017 and 2018 represent a pond density of 0.3 and 0.4% respectively of the debris-covered area, and although they experienced variations in volume, their total water volume increased by 50,924 m^3.

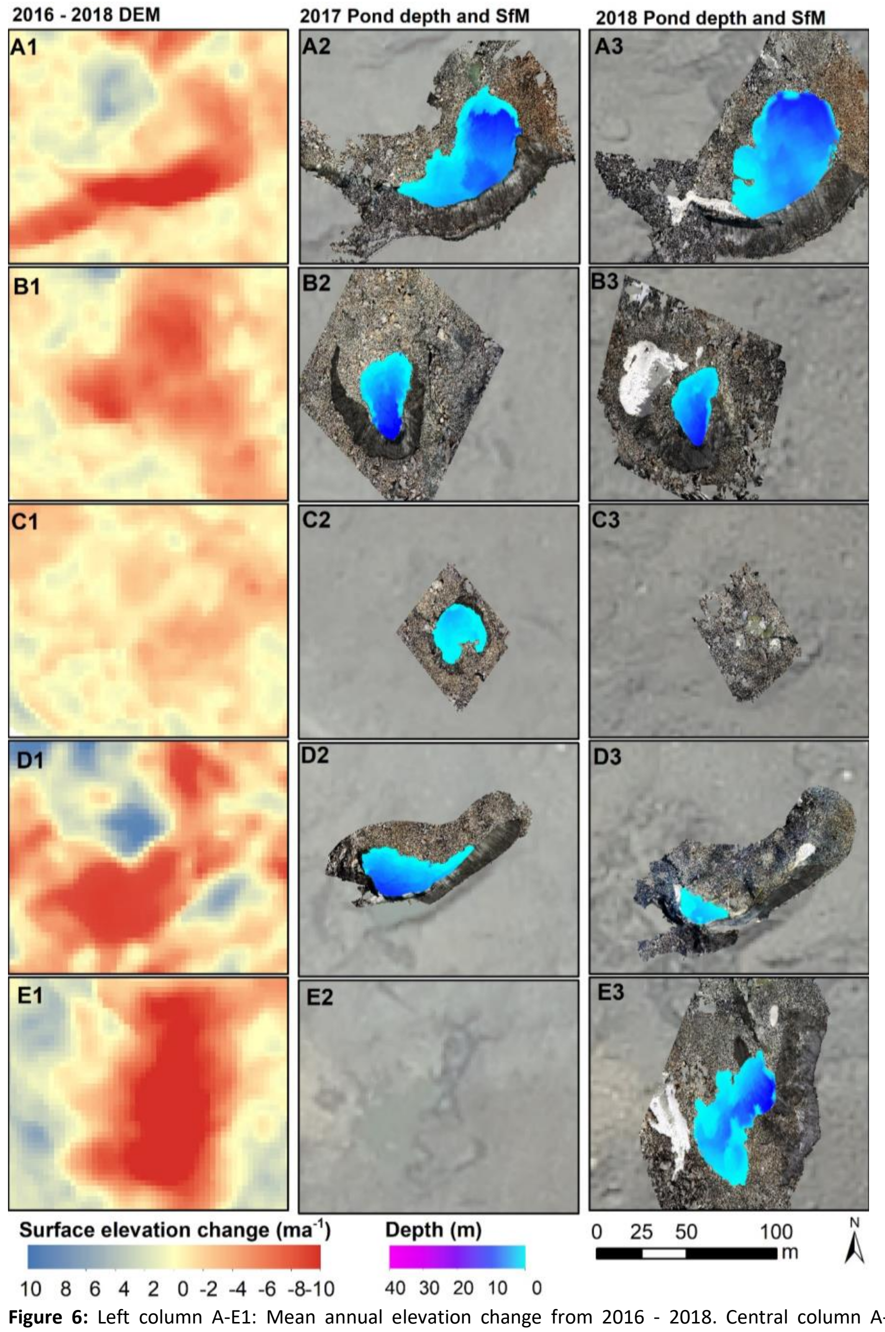

Figure 6: Left column A-E1: Mean annual elevation change from 2016 - 2018. Central column A-E2: Bathymetry and photogrammetry surveys in 2017 with SPOT7 orthophoto background. Right column A-E3: Bathymetry and photogrammetry surveys in 2018 with SPOT7 orthophoto background.

Lake Miage increased in both area and volume from 2017 to 2018, expanding from 11,931 m^2 to 16,028 m^2 despite a reduction in maximum depth of 6.38 m. A drainage event of Lake Miage occurred in September 2018 with photographic evidence showing substantial reduction in water level (Figure 7). It is understood that the drainage occurred over the course of a few days between approximately 25/09/2018 and 29/09/2018 resulting in the reduction of water level from the notch line, identifiable in the image via a conduit at the eastern end of the lake. The lake drained an estimated ~102,000 m^3 based on the assumption the bathymetry remained stable since the survey in the previous July.

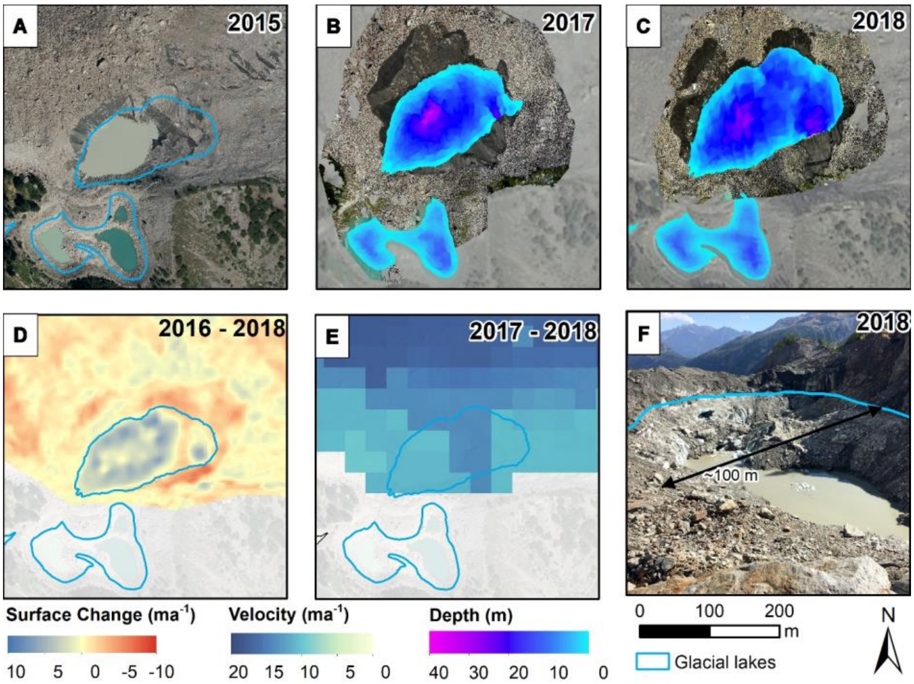

Figure 7: A: Lake Miage in 2015 TerraItaly orthoimage with lake outline of 2018 extent. B: Lake Miage bathymetric survey and photogrammetry surveys in 2017. C: Lake Miage bathymetric survey and photogrammetry surveys in 2018. D: Elevation change from 2016 – 2018. E: Surface velocity from 2017 – 2018. F: Drainage at the end of the ablation season October 2018; Photo credit: Connor Downes.

All ponds were surrounded in part by north-facing cliffs (Figure 6). Part of the ice cliff surrounding Lake Miage, also faced a southerly direction, which was observed with a lower surface slope (8 - 10°) in comparison to the north-facing slope (26 - 29°) in both the 2017 and 2018 surveys (Table 11).

Table 11: Summary of 2017 and 2018 ice cliff geometry results.

Model		Max. height of ice cliff (m)	Surface Area (m^2)	Aspect (°)	Mean surface slope (°)
Lake Miage (N/S)	2017	32.29	10406	336 / 162	26 / 8
	2018	42.22	11615	338 / 154	29 / 10
S1	2017	26.64	2346	358	23
	2018	29.6	1692	356	29
S2	2017	13.24	943	035	10
	2018	18.29	1807	057	16
S3	2017	4.79	165	022	2
	2018	-	-	-	-
S4	2017	15.76	1055	325	12
	2018	15.40	864	277	6
S5	2017	-	-	-	-
	2018	24.8	1728	283	18

The ice cliffs retreated substantially ranging from -0.93 m a^{-1} to 8.15 m a^{-1} (Table 12), equating to a volumetric ice loss of 39,569 m^3 between 2017 and 2018 and approximately 2% of the total glacier geodetic mass balance during this period. The highest ice cliff retreat rates occurred around the margins of S4 (-8.15 m a^{-1}) and S1 (-5.24 m a^{-1}) respectively (Table 12), particularly around north-facing slopes. The northern-facing Lake Miage ice cliffs experienced higher melt rates in comparison to the southern-facing cliff and was observed to have migrated further onto the glacier.

Table 12: Mean ice cliff retreat rates between the 2017 and 2018 surveys assessed through the M3C2 algorithm. Annual retreat rates were standardised as the survey dates were not exactly 1 year apart.

Lake	Mean M3C2 distance (m)	St Deviation (m)	Mean annual retreat rate (m)	Volume ice lost (m^3)	Mean daily retreat rates (cm d^{-1})	Total Error (E_T) (m)
Miage N	-2.70	2.62	-2.79	14048	-0.76	0.26
Miage S	-0.91	2.35	-0.93	1067	-0.26	0.26
S1	-5.12	3.72	-5.24	12011	-1.44	0.83
S2	-2.41	2.44	-2.47	4077	-0.68	1.00
S3	-	-	-	-	-	1.05
S4	-7.93	1.69	-8.15	8366	-2.23	1.01

5. Discussion

5.1. Recent and long-term evolution of Miage Glacier

Previous studies have detailed how Miage Glacier has evolved over the period 1913 to 1999 (Smiraglia et al., 2000; Thomson et al., 2000). Our data provide an update to those observations through a period of continued climate warming, and the combined results represent a rare opportunity to examine debris-covered glacier dynamics across annual, decadal and centennial timescales. Thomson et al. (2000) and Smiraglia et al. (2000) described spatially and temporally complex patterns of change through the twentieth century; overall patterns of thinning and modest terminal recession since the LIA maximum were punctuated by a brief period of centreline and terminal thickening and a small advance during the late twentieth century in response to positive mass balances between the 1960s to 1980s, as observed elsewhere in the Alps (Diolaiuti et al., 2003; Huss, 2012). With reference to the 3-stage debris-covered glacier evolution model of Benn et al. (2012), Miage Glacier was consistent with 'Regime 1' during the twentieth century (Thomson et al., 2000) in that it experienced widespread active ice flow, with limited water storage on the glacier surface. Over the period 1990 to 2018, our data reveal that Miage Glacier has transitioned into 'Regime 2', characterised by downwasting ice, surface water storage, expanding debris cover, and glacier slowdown.

In terms of volumetric changes, there has been only modest overall area loss (-11%) (Table 7) and a small amount of recession of the terminal lobes (of ~50 ± 10.96 m), but there are notably more substantial local area losses in the tributary glaciers that feed Miage's main trunk (Figures 2, 3, and 4). There has been continued and pervasive thinning, although the rate of thinning appears to have slowed overall (Table 8; Figure 3), possibly as a consequence of the expanding and suspected thickening debris cover that has the effect of slowing ablation rates. However, the most recent results show that the trend of thinning is non-linear, with mass loss of -0.35 ± 0.10 m w.e. a^{-1} between 2012 and 2014, and a higher rate of -0.64 ± 0.20 w.e. a^{-1} between 2016 and 2018 (Table 8). In response to this continued thinning across the glacier, the longitudinal gradient of the centreline has reduced modestly over the study period from 6.63 to 5.91° (Figure 8). Furthermore, the valley section from the base of Bionnassay Glacier to the top of the terminal lobes has changed very little from 5.21 to 5.15°.

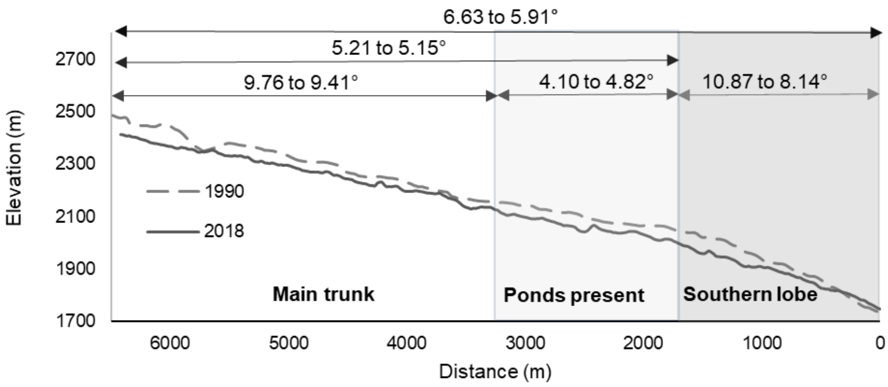

Figure 8: Longitudinal profile of the glacier centreline in 1990 and 2018.

In terms of surface changes, debris cover has expanded by 0.38 km^2 up-glacier through the study period, increasing from 43% to 52% of the total glacier surface area (Figures 2 and 5; Table 7). Notably, supraglacial ponds have begun to emerge on the surface of Miage Glacier and now cover >6000 m^2, whilst ice cliffs have increased in area by 184% since 1990 (Figure 2 and 5; Table 7). Furthermore, Miage Glacier has slowed substantially (by ~46% on average) from 34 ± 0.05 m a^{-1} in 1990 to 16 ± 0.05 m a^{-1} in 2018, with near-stagnant flow rates on the terminal lobes (<3 m a^{-1}) (Figure 4).

These observations are broadly consistent with the evolution of debris-covered glaciers elsewhere that are experiencing negative mass balances in response to climate change, although with some key differences and complexities (e.g. Benn et al., 2012; Benn and Lehmkuhl, 2000; Bolch et al., 2012; Rowan et al., 2015; Scherler et al., 2011). Reduced flow rates and progressive stagnation are being driven by reduced inputs and progressive disconnection from tributary glaciers (exemplified by the rapid thinning of the Mont Blanc Glacier base where it connects to Miage Glacier; Figure 3f), as well as thinning and flattening on the main tongue, which has the effect of reducing shear stress and internal deformation rates (e.g. Dehecq et al., 2019; Quincey et al., 2009). Less vigorous flow and sustained negative mass balance means that Miage Glacier struggles to evacuate debris that is sourced from valley slopes and that melts-out from englacial septa (e.g. Kirkbride and Deline, 2013). Consequently, the supraglacial debris cover has progressively thickened and extended further upglacier. Progressive thinning, flattening, slowing, and a reduction in the efficiency of meltwater evacuation has led to the development of supraglacial ponds and associated ice cliffs in recent years, representing localised hotspots of ablation (Figures 5, 6 and 7; Tables 9, 10, 11 and 12; Benn et al., 2012).

5.2. Regional and global comparisons

Our mass balance results highlight the importance of a surface debris cover in moderating glacier response to climatic change, but also that debris-covered glacier responses can themselves be highly variable. Broadly, the negative mass balance of Miage Glacier is consistent with results from other studies in the Mont Blanc massif and the Alps more generally (Berthier et al., 2014; Huss, 2012; Mölg et al., 2019; Paul et al., 2007; Rabatel et al., 2016; Vincent et al., 2017; Zekollari et al., 2020). Between 2003 and 2012, mass loss from Miage Glacier was 19% lower (−0.84 ± 0.22 m w.e. a^{-1}) than the Mont Blanc region average, which includes a number of clean-ice glaciers where rates of mass loss have been higher (Berthier et al., 2014). Across the European Alps more broadly, our 1990-2008 average geodetic mass balance (-0.88 m w.e. a^{-1}; Table 8) is similar to the mean annual mass balance of -0.83 m w.e. a^{-1} between 1990 – 2010 calculated from decadal means for the Swiss Alps (Huss et al., 2015).

The presence of a continuous, thick debris cover at Miage Glacier appears to retard mass loss compared to nearby clean-ice glaciers, and the most rapid thinning rates are currently focussed around supraglacial ponds and ice cliffs (Mölg et al., 2019; Reid and Brock, 2014; Sakai et al., 2000; Thompson et al., 2016). Similar to the 1990-2018 trend at Miage Glacier, the debris-covered Glacier de Tsarmine also exhibited a deceleration of lowering rates since 1999 despite increasing air temperatures (Capt et al., 2016). By contrast, Zmuttgletscher in Switzerland, has a thinner and less extensive debris cover, and was found to exhibit similar mass loss to clean-ice glaciers; although supraglacial ponds were few and their influence on ablation not analysed (Mölg et al., 2019). These seemingly contradictory results highlight the complexity of responses to climate change, not just when comparing ablation rates of debris-covered glaciers with clean-ice glaciers, but also when comparing the responses of different debris-covered glaciers to one another (e.g. Pellicciotti et al., 2015; Salerno et al., 2017; Vincent et al., 2016).

The reasons behind the most recent 2016-2018 intensification in thinning rates at Miage Glacier compared to 2012-2014 (from 1990-2008 to 2008-2018) are unclear (Table 8), but the results highlight the non-linear nature of ablation of debris-covered glaciers. One possibility is a lagged response to temperature and precipitation changes and associated changes in ice flux, as seen elsewhere (e.g. Kääb et al., 2012; Senese et al., 2012). Continued monitoring will be required to assess to what extent this represents a longer-term trend of enhanced thinning rates, or merely a brief deviation.

Our observation that Miage Glacier has slowed over the course of our monitoring period is consistent with similar findings from across the European Alps, including Switzerland (Capt et al., 2016; Mölg et al., 2019), Austria (Kellerer‐Pirklbauer and Kulmer, 2019), and France (Vincent et al., 2009). Likewise, the increasing debris cover at Miage Glacier is similar to that seen since the 1990s on Zmuttgletscher (Mölg et al., 2019) and on the glaciers of the Ortles-Cevedale Group, Italy (Azzoni et al., 2018).

The recent emergence and growth of supraglacial ponds and ice cliffs on Miage Glacier is a particularly striking surface expression of the transition to 'Regime 2' of the debris-covered glacier evolution model (Benn et al., 2012). These features have played an important role in the glacier's mass balance, and may continue to do so in the future. Specifically, there is a spatial coincidence between areas of rapid thinning and the locations of ice cliffs and ponds (Figure 4 and 5), and these features contribute disproportionately to ablation, as has been reported for other sites globally (Brun et al., 2016; Immerzeel et al., 2014; Miles et al., 2017a; 2018; Nicholson and Benn, 2006; Pellicciotti et al., 2015; Ragettli et al., 2015; Sakai et al., 2002; Thompson et al., 2016). Mapped ice cliffs between 2016 and 2018 account for ~4% of total geodetic mass loss yet only account for ~1% of the total glacier area, although there has been a reduction in cliff density and contribution to negative mass balance since 2012-2014 (Table 9). Nonetheless, these results are comparable to those of Reid and Brock (2014) who found that modelled ice cliff ablation on Miage Glacier during 2010 - 2011 accounted for ~7.4% of total ablation, despite only covering 1.3% of the glacier area. Likewise, at Zmuttgletscher, Switzerland, ice cliffs were found to cover up to 1.8% of the debris-covered area, yet drove 5% of glacier-wide volume loss (Mölg et al., 2019). However, these figures for glaciers in the European Alps are substantially lower than those found on Lirung Glacier, Ngozumpa Glacier and

Changri Nup Glacier in the Himalaya where ice cliff backwasting accounted for 69%, 40% and 23% of the total mass loss respectively despite a comparatively small area coverage (2%, 5% and 7% respectively) (Brun et al., 2018; Sakai et al., 1998; Thompson et al., 2016). Such disparity between the Alpine and Himalayan examples suggest substantial regional variations of contributions of ice cliffs to mass loss.

Supraglacial ponds at Miage Glacier contributed between 0.58 and 1.19% of the geodetic mass loss in the 2012-2018 study period, despite only covering between 0.27 and 0.15% of glacier area respectively. These values are lower than that contributed by ice cliffs, explained in part by the lower density of ponds across the glacier surface (Table 9). Although, there are no comparable data on supraglacial pond-related glacier ablation in the Alps, by comparison, in the Langtang region of Nepal, up to 12.5% of glacier ablation is driven by supraglacial ponds, despite ponds only covering 1.69% of the debris-covered area (Miles et al., 2018). This disproportionate ablation rate per unit area coverage is similar in magnitude to the 2012-2014 values at Miage (Table 9; i.e. ablation percentage is around 7.4 to 7.9 times the percentage of glacier area cover). However, at Miage Glacier, there is an apparent slowdown in the contribution of supraglacial ponds to geodetic mass balance loss from 2012-2014 to 2016-2018 (Table 9).

Many ponds on Miage Glacier, and other debris-covered glaciers, are coeval with adjacent ice cliffs (e.g. Thompson et al., 2016; Watson et al., 2017a). Together, supraglacial ponds and ice cliffs covered between 1.2 to 1.5% of the total glacier area but were typically responsible for a disproportionately large amount of the net annual mass loss, ranging from 5 to 10% of the overall ablation between 2012 and 2018 (Table 9). However, the contribution of supraglacial ponds and ice cliffs to the geodetic mass balance is likely to be underrepresented in our study because ablation rates distal to these focal points are not quantified.

The first-order DEM-differencing technique cannot capture the full range of ice cliff and pond dynamics, but our field-based photogrammetry and bathymetric surveys reveal additional details of how important these features might be for the evolution of Miage Glacier. Photogrammetric surveys undertaken in 2017 and 2018 show that ice cliff backwastage resulted in an annual ice loss of 39,569 m^3 for the five ice cliffs surveyed, which accounted for 0.3 – 0.4% of the debris-covered area; ice cliff retreat rates reached up to 8.15 m a^{-1} (Table 12). Bathymetric surveys showed that supraglacial ponds increased in water volume by

50,924 m^3 between 2017 and 2018 (Table 10), and now comprise 8% of the water stored on or around the margins of Miage Glacier. Nonetheless, the results indicate high interannual variability whereby some individual ponds grow substantially, whilst others disappear (Table 10). This is consistent with other studies of pond dynamics. For example, Miles et al. (2017b) observed high levels of seasonal and interannual variability of ponds with many appearing in the pre-monsoon season as snow melts. In the Alps, ponds are expected to form at the start of the ablation period from high levels of snow melt, and decline towards the end of the ablation season when englacial connectivity and hydrological pathways open (Fyffe et al., 2019); longer-term monitoring of pond dynamics will be required to assess seasonal and annual variability in water storage and contribution to ablation.

5.3. Future prognosis for Miage Glacier

Given that climate predictions suggest that temperatures will increase (Sherwood et al., 2020), it is anticipated that Miage Glacier will continue to experience negative mass balance in the future. Based on extrapolation of dynamic trends outlined in this study since 1990, we suggest that Miage Glacier will continue to thin, that the glacier will continue to slow, and that debris cover will continue to expand upglacier, as well as thicken.It is also possible that the overall glacier profile will become shallower although changes in the gradient have been relatively modest since 1975 (Smiraglia et al., 2000). Ablation is likely to be enhanced at the base of the tributary glaciers resulting in thinning and eventual decoupling and recession from the main stem of Miage Glacier. Reduced inputs of ice will likely lead to further reductions in surface velocity and stagnation, which will promote flattening and the inability of the main glacier trunk to evacuate englacial and supraglacial sediment. Indeed, it is also likely that sediment inputs from valley sides will be enhanced with continued climate warming (Deline, 2009; Ravanel et al., 2017), further promoting expansion and thickening of the debris cover. Although a thicker and more extensive debris cover has the potential to reduce ablation, glaciers in the Himalaya have shown similar mass loss to clean-ice glaciers referred to as the debris-cover anomaly (Pellicciotti et al., 2015). Despite this, it is unlikely to occur at Miage Glacier since the development of ice cliffs and supraglacial ponds promote regions of enhanced localised ablation.

Extrapolation of other trends and elements of our dataset become far more speculative because of the non-linear changes evident in some of our datasets. Perhaps most notable among these uncertainties is the future role that supraglacial ponds and adjacent ice cliffs might play in glacier mass balance. It is evident from our dataset that ponds and ice cliffs represent ablation hotspots. However, their current distribution is limited to a relatively small zone upglacier from the terminal lobes where the main trunk turns into Val Veny (Figure 5). Even within this zone, ponds and ice cliffs are highly focussed and are not pervasive features at present and are thus unlikely to counteract the reduction in ablation from the debris cover. A key limitation on their future development will be that the glacier remains, overall, relatively steep (~5° on the valley tongue and >8° on the terminal lobes (Figure 8) (e.g. Quincey et al., 2007; Reynolds, 2000). In accordance with observations on other debris-covered glaciers (e.g. Benn et al., 2012; Rowan et al., 2015), there is evidence that thinning of the terminal lobes is reducing under a thickening debris cover, and that ablation is focused in the cleaner ice zone at the base of the tributary glaciers, with the overall effect of flattening the glacier profile (Smiraglia et al., 2000). Further slowdown of the glacier may also be conducive to pond development (Quincey et al., 2007). Our data show that changes in ice cliffs and ponds, and their contributions to mass balance, are very complex and will require continued monitoring to unravel their overall significance for the future of the glacier. On the one hand, water storage in supraglacial ponds has increased, as has pond density; on the other hand, pond contribution to ablation has slowed. Likewise, ice cliff back-wasting can be substantial (up to 8.15 m a^{-1}), but ice cliff density and contribution to ablation have both reduced recently.

The development of surface ponds and ice cliffs has been shown to be very important for the evolution and down-wasting of debris-covered glaciers in other locations (e.g. Benn et al., 2012; Pellicciotti et al., 2015; Thompson et al., 2016; Watson et al., 2017b). In the Himalaya, the development and coalescence of ponds, and the ultimate development of a moraine-dammed proglacial or supraglacial lake characterises 'Regime 3' in the model of Benn et al. (2012). It is also notable that ablation rates associated with ice cliffs are much lower for Miage than for Himalayan glaciers (e.g. Thompson et al., 2016; Watson et al., 2017b). Ultimately, it is unclear whether Miage Glacier will develop toward this phase, but it does not appear to be transitioning to Regime 3 currently or in the near future and may remain in Regime 2 for the foreseeable future.

6. Conclusions

This study provides an integrated assessment of multi-decadal (1990-2018) changes in geodetic mass balance, debris cover, surface velocity, and the roles of supraglacial pond and ice cliff development on Miage Glacier, Mont Blanc Massif, Italy. Miage Glacier has transitioned from a period of active flow and limited surface water storage during the twentieth century to one of downwasting ice with continued thinning since 1990 (-0.86 ± 0.27 m w.e. a^{-1}), increased surface water storage (+50,924 m^3 between 2017 to 2018), expanded debris cover (+0.34 km^2, 1990 - 2018) and a dramatic reduction in glacier surface velocity from a mean of 34 ± 0.05 m a^{-1} in 1990 to 16 ± 0.05 m a^{-1} in 2018. During the observation period, Miage Glacier has undergone significant widespread downwasting although surface lowering has slowed from -1.07 ± 0.13 m a^{-1} between 1990 and 2008, to -0.85 ± 0.01 m a^{-1} between 2008 and 2018, which is attributed to an expanding debris cover. Despite the long-term negative mass balance, recent surface lowering results show a deceleration in thinning indicating complex, non-linear changes over time. The presence of supraglacial ponds and ice cliffs serve to enhance mass loss locally and were responsible for ~5% of the total mass loss between 2016 and 2018, despite only covering 1.3% of the total glacier area.

With reference to other studies in the Alps and other high-mountain regions, this study illustrates the varied and complex response of debris-covered glaciers to climatic change. In general, Miage Glacier is entering a more advanced state of decay although the contributions of ponds and ice cliffs to total mass loss are comparably lower than for Himalayan glaciers; Miage Glacier remains relatively steep limiting future expansion of supraglacial ponds and their associated ice cliffs.

In the future, it is expected that Miage Glacier will continue to thin, further stagnate, and that debris cover will continue to expand upglacier, as well as thicken. The main trunk of the glacier continues to show signs of active flow albeit at a much-reduced rate; however, our mapping indicates progressive separation of the Mont Blanc tributary glacier. If the tributaries become severed from the main trunk, then this would have a profound impact in terms of increasing the rate of decay and downwasting of the main trunk. The contribution of supraglacial ponds and ice cliffs to mass balance are complex and require continued assessment in the coming years especially as their influence on ablation could increase if the glacier were to slow and flatten further.

Acknowledgments

This study was funded by Nottingham Trent University as part of PhD research. We would like to thank the European Space Agency who provided access to the SPOT and Pleiades data under proposal 35359. Thanks also go to those who have helped on various field visits including Guaduneth Chico, Daniel Fitter, Miles Shirtcliffe, Bethany Bird, Mark Chaney-Baxter and Emma Higginbotham. Thanks also go to the reviewers whose comments have significantly improved this manuscript.

References

Anderson, L.S., Anderson, R.S., 2018. Debris thickness patterns on debris-covered glaciers. Geomorphology 311, 1–12. https://doi.org/10.1016/j.geomorph.2018.03.014

Anderson, L.S., Anderson, R.S., 2016. Modeling debris-covered glaciers: response to steady debris deposition. The Cryosphere 10, 1105–1124. https://doi.org/10.5194/tc-10-1105-2016

Azzoni, R.S., Fugazza, D., Zerboni, A., Senese, A., D'Agata, C., Maragno, D., Carzaniga, A., Cernuschi, M., Diolaiuti, G.A., 2018. Evaluating high-resolution remote sensing data for reconstructing the recent evolution of supra glacial debris: A study in the Central Alps (Stelvio Park, Italy). Prog. Phys. Geogr. Earth Environ. 42, 3–23. https://doi.org/10.1177/0309133317749434

Baltsavias, E., Kocaman, S., Akca, D., Wolff, K., 2007. Geometric and radiometric investigations of Cartosat-1 data, in: ISPRS Workshop" High Resolution Earth Imaging for Geospatial Information". ISPRS.

Bash, E.A., Moorman, B.J., Gunther, A., 2018. Detecting Short-Term Surface Melt on an Arctic Glacier Using UAV Surveys. Remote Sens. 10, 1547. https://doi.org/10.3390/rs10101547

Benn, D.I., Bolch, T., Hands, K., Gulley, J., Luckman, A., Nicholson, L.I., Quincey, D., Thompson, S., Toumi, R., Wiseman, S., 2012. Response of debris-covered glaciers in the Mount Everest region to recent warming, and implications for outburst flood hazards. Earth-Sci. Rev. 114, 156–174. https://doi.org/10.1016/j.earscirev.2012.03.008

Benn, D.I., Lehmkuhl, F., 2000. Mass balance and equilibrium-line altitudes of glaciers in high-mountain environments. Quat. Int. 65–66, 15–29. https://doi.org/10.1016/S1040-6182(99)00034-8

Benn, D.I., Wiseman, S., Hands, K.A., 2001. Growth and drainage of supraglacial lakes on debris mantled Ngozumpa Glacier, Khumbu Himal, Nepal. J. Glaciol. 47, 626–638. https://doi.org/10.3189/172756501781831729

Berthier, E., Vincent, C., Magnússon, E., Gunnlaugsson, Á., Pitte, P., Le Meur, E., Masiokas, M., Ruiz, L., Pálsson, F., Belart, J.M.C., 2014. Glacier topography and elevation changes derived from Pléiades sub-meter stereo images. Cryosphere 8, 2275–2291. https://doi.org/10.5194/tc-8-2275-2014

Berthier, E., Cabot, V., Vincent, C., Six, D., 2016. Decadal Region-Wide and Glacier-Wide Mass Balances Derived from Multi-Temporal ASTER Satellite Digital Elevation Models. Validation over the Mont-Blanc Area. Front. Earth Sci. 4. https://doi.org/10.3389/feart.2016.00063

Bolch, T., Kulkarni, A., Kaab, A., Huggel, C., Paul, F., Cogley, J.G., Frey, H., Kargel, J.S., Fujita, K., Scheel, M., Bajracharya, S., Stoffel, M., 2012. The State and Fate of Himalayan Glaciers. Science 336, 310–314. https://doi.org/10.1126/science.1215828

Bolch, T., Pieczonka, T., Benn, D.I., 2011. Multi-decadal mass loss of glaciers in the Everest area (Nepal Himalaya) derived from stereo imagery. The Cryosphere 5, 349–358. https://doi.org/10.5194/tc-5-349-2011

Brock, B.W., Mihalcea, C., Kirkbride, M.P., Diolaiuti, G., Cutler, M.E.J., Smiraglia, C., 2010. Meteorology and surface energy fluxes in the 2005–2007 ablation seasons at the Miage debris-covered glacier, Mont Blanc Massif, Italian Alps. J. Geophys. Res. Atmospheres 115, D09106. https://doi.org/10.1029/2009JD013224

Brun, F., Buri, P., Miles, E.S., Wagnon, P., Steiner, J., Berthier, E., Ragettli, S., Kraaijenbrink, P., Immerzeel, W.W., Pellicciotti, F., 2016. Quantifying volume loss from ice cliffs on debris-covered glaciers using high-resolution terrestrial and aerial photogrammetry. J. Glaciol. 62, 684–695. https://doi.org/10.1017/jog.2016.54

Brun, F., Wagnon, P., Berthier, E., Shea, J.M., Immerzeel, W.W., Kraaijenbrink, P.D.A., Vincent, C., Reverchon, C., Shrestha, D., Arnaud, Y., 2018. Ice cliff contribution to the tongue-wide ablation of Changri Nup Glacier, Nepal, central Himalaya. The Cryosphere 12, 3439–3457. https://doi.org/10.5194/tc-12-3439-2018

Capt, M., Bosson, J.-B., Fischer, M., Micheletti, N., Lambiel, C., 2016. Decadal evolution of a very small heavily debris-covered glacier in an Alpine permafrost environment. J. Glaciol. FirstView, 1–17. https://doi.org/10.1017/jog.2016.56

Cheng, P., 2015. Pan-Sharpening, DEM Extraction and Geometric Correction - Spot-6 and Spot-7 Satellites. GeoInformatics 18, 24.

Conforti, D., Deline, P., Mortara, G., Tamburini, A., 2005. Terrestrial scanning LiDAR technology applied to study the evolution of the ice-contact Miage lake (Mont Blanc, Italy), in: Proceedings of the 9th Alpine Glaciological Meeting. Milan, Italy. https://doi.org/10.1.1.503.4137

Dehecq, A., Gourmelen, N., Gardner, A.S., Brun, F., Goldberg, D., Nienow, P.W., Berthier, E., Vincent, C., Wagnon, P., Trouvé, E., 2019. Twenty-first century glacier slowdown driven by mass loss in High Mountain Asia. Nat. Geosci. 12, 22–27. https://doi.org/10.1038/s41561-018-0271-9

Deline, P., 2009. Interactions between rock avalanches and glaciers in the Mont Blanc massif during the late Holocene. Quat. Sci. Rev., Natural Hazards, Extreme Events and Mountain Topography 28, 1070–1083. https://doi.org/10.1016/j.quascirev.2008.09.025

Deline, P., 2005. Change in surface debris cover on Mont Blanc massif glaciers after the 'Little Ice Age' termination. The Holocene 15, 302–309. https://doi.org/10.1191/0959683605hl809rr

Diolaiuti, G., Citterio, M., Carnielli, T., D'Agata, C., Kirkbride, M., Smiraglia, C., 2006. Rates, processes and morphology of freshwater calving at Miage Glacier (Italian Alps). Hydrol. Process. 20, 2233–2244. https://doi.org/10.1002/hyp.6198

Diolaiuti, G., D'Agata, C., Meazza, A., Zanutta, A., Smiraglia, C., 2009. Recent (1975–2003) changes in the Miage debris-covered glacier tongue (Mont Blanc, Italy) from analysis of aerial photos and maps. Geogr. Fis. E Din. Quat. 32, 117–127.

Diolaiuti, G., D'Agata, C., Smiraglia, C., 2003. Belvedere Glacier, Monte Rosa, Italian Alps: Tongue Thickness and Volume Variations in the Second Half of the 20th Century. Arct. Antarct. Alp. Res. 35, 255–263. https://doi.org/10.1657/1523-0430(2003)035[0255:BGMRIA]2.0.CO;2

Diolaiuti, G., Kirkbride, M.P., Smiraglia, C., Benn, D.I., D'Agata, C., Nicholson, L., 2005. Calving processes and lake evolution at Miage glacier, Mont Blanc, Italian Alps. Ann. Glaciol. 40, 207–214. https://doi.org/10.3189/172756405781813690

Falaschi, D., Lenzano, M.G., Villalba, R., Bolch, T., Rivera, A., Lo Vecchio, A., 2019. Six Decades (1958–2018) of Geodetic Glacier Mass Balance in Monte San Lorenzo, Patagonian Andes. Front. Earth Sci. 7. https://doi.org/10.3389/feart.2019.00326

Fyffe, C., Reid, T., Brock, B., Kirkbride, M., Diolaiuti, G., Smiraglia, C., Diotri, F., 2014. A distributed energy-balance melt model of an alpine debris-covered glacier. J. Glaciol. 60, 587–602. https://doi.org/10.3189/2014JoG13J148
Fyffe, C.L., Brock, B.W., Kirkbride, M.P., Mair, D.W.F., Arnold, N.S., Smiraglia, C., Diolaiuti, G., Diotri, F., 2019. Do debris-covered glaciers demonstrate distinctive hydrological behaviour compared to clean glaciers? J. Hydrol. 570, 584–597. https://doi.org/10.1016/j.jhydrol.2018.12.069
Fyffe, C.L., Woodget, A.S., Kirkbride, M.P., Deline, P., Westoby, M.J., Brock, B.W., 2020. Processes at the margins of supraglacial debris cover: quantifying dirty ice ablation and debris redistribution. Earth Surf. Process. Landf. n/a. https://doi.org/10.1002/esp.4879
Gardelle, J., Berthier, E., Arnaud, Y., Kaab, A., 2013. Region-wide glacier mass balances over the Pamir-Karakoram-Himalaya during 1999-2011. The Cryosphere 7, 1885–1886. https://doi.org/10.5194/tc-7-1885-2013
Gibson, M.J., Glasser, N.F., Quincey, D.J., Mayer, C., Rowan, A.V., Irvine-Fynn, T.D.L., 2017. Temporal variations in supraglacial debris distribution on Baltoro Glacier, Karakoram between 2001 and 2012. Geomorphology 295, 572–585. https://doi.org/10.1016/j.geomorph.2017.08.012
Hall, D.K., Bayr, K.J., Schöner, W., Bindschadler, R.A., Chien, J.Y.L., 2003. Consideration of the errors inherent in mapping historical glacier positions in Austria from the ground and space (1893–2001). Remote Sens. Environ. 86, 566–577. https://doi.org/10.1016/S0034-4257(03)00134-2
Hambrey, M.J., Quincey, D.J., Glasser, N.F., Reynolds, J.M., Richardson, S.J., Clemmens, S., 2008. Sedimentological, geomorphological and dynamic context of debris-mantled glaciers, Mount Everest (Sagarmatha) region, Nepal. Quat. Sci. Rev. 27, 2361–2389. https://doi.org/10.1016/j.quascirev.2008.08.010
Heid, T., Kääb, A., 2012. Evaluation of existing image matching methods for deriving glacier surface displacements globally from optical satellite imagery. Remote Sens. Environ. 118, 339–355. https://doi.org/10.1016/j.rse.2011.11.024
Huss, M., 2013. Density assumptions for converting geodetic glacier volume change to mass change. The Cryosphere 7, 877–887. https://doi.org/10.5194/tc-7-877-2013
Huss, M., 2012. Extrapolating glacier mass balance to the mountain-range scale: the European Alps 1900–2100. The Cryosphere 6, 713–727. https://doi.org/10.5194/tc-6-713-2012
Huss, M., Dhulst, L., Bauder, A., 2015. New long-term mass-balance series for the Swiss Alps. J. Glaciol. 61, 551–562. https://doi.org/10.3189/2015JoG15J015
Immerzeel, W.W., Kraaijenbrink, P.D.A., Shea, J.M., Shrestha, A.B., Pellicciotti, F., Bierkens, M.F.P., de Jong, S.M., 2014. High-resolution monitoring of Himalayan glacier dynamics using unmanned aerial vehicles. Remote Sens. Environ. 150, 93–103. https://doi.org/10.1016/j.rse.2014.04.025
IPCC, 2014. Climate Change 2014: Synthesis Report. Contribution of Working Groups I, II and III to the Fifth Assessment Report of the Intergovernmental Panel on Climate Change [Core Writing Team, R.K. Pachauri and L.A. Meyer (eds.)]. IPCC, Geneva, Switzerland, 151 pp. [WWW Document]. URL http://www.ipcc.ch/report/ar5/syr/ (accessed 8.31.16).
Kääb, A., 2005. Combination of SRTM3 and repeat ASTER data for deriving alpine glacier flow velocities in the Bhutan Himalaya. Remote Sens. Environ. 94, 463–474. https://doi.org/10.1016/j.rse.2004.11.003
Kääb, A., Berthier, E., Nuth, C., Gardelle, J., Arnaud, Y., 2012. Contrasting patterns of early twenty-first-century glacier mass change in the Himalayas. Nature 488, 495–498. https://doi.org/10.1038/nature11324
Kääb, A., Vollmer, M., 2000. Surface Geometry, Thickness Changes and Flow Fields on Creeping Mountain Permafrost: Automatic Extraction by Digital Image Analysis. Permafr. Periglac. Process. 11, 315–326. https://doi.org/10.1002/1099-1530(200012)11:4<315::AID-PPP365>3.0.CO;2-J
Kellerer-Pirklbauer, A., Kulmer, B., 2019. The evolution of brittle and ductile structures at the surface of a partly debris-covered, rapidly thinning and slowly moving glacier in 1998–2012 (Pasterze Glacier, Austria). Earth Surf. Process. Landf. 44, 1034–1049. https://doi.org/10.1002/esp.4552
King, O., Quincey, D.J., Carrivick, J.L., Rowan, A.V., 2017. Spatial variability in mass loss of glaciers in the Everest region, central Himalayas, between 2000 and 2015. The Cryosphere 11, 407–426. https://doi.org/10.5194/tc-11-407-2017

Formatted: English (United Kingdom)

Kirkbride, M.P., Deline, P., 2013. The formation of supraglacial debris covers by primary dispersal from transverse englacial debris bands. Earth Surf. Process. Landf. 38, 1779–1792. https://doi.org/10.1002/esp.3416

Lague, D., Brodu, N., Leroux, J., 2013. Accurate 3D comparison of complex topography with terrestrial laser scanner: Application to the Rangitikei canyon (N-Z). ISPRS J. Photogramm. Remote Sens. 82, 10–26. https://doi.org/10.1016/j.isprsjprs.2013.04.009

Masetti, M., Diolaiuti, G., D'Agata, C., Smiraglia, C., 2010. Hydrological Characterization of an Ice-Contact Lake: Miage Lake (Monte Bianco, Italy). Water Resour. Manag. 24, 1677–1696. https://doi.org/10.1007/s11269-009-9519-x

Mattson, L.E., Gardner, J.S., Young, G.J., 1993. Ablation on debris covered glaciers: an example from the Rakhiot Glacier, Punjab, Himalaya, in: Young, G.J. (Ed.), Snow and Glacier Hydrology. IAHS-IASH Publication 218, Wallingford, pp. 289–296.

McFeeters, S.K., 1996. The use of the Normalized Difference Water Index (NDWI) in the delineation of open water features. Int. J. Remote Sens. 17, 1425–1432. https://doi.org/10.1080/01431169608948714

Midgley, N.G., Tonkin, T.N., 2017. Reconstruction of former glacier surface topography from archive oblique aerial images. Geomorphology 282, 18–26. https://doi.org/10.1016/j.geomorph.2017.01.008

Miles, E.S., Pellicciotti, F., Willis, I.C., Steiner, J.F., Buri, P., Arnold, N.S., 2016. Refined energy-balance modelling of a supraglacial pond, Langtang Khola, Nepal. Ann. Glaciol. 57, 29. https://doi.org/10.3189/2016AoG71A421

Miles, E.S., Steiner, J., Willis, I., Buri, P., Immerzeel, W.W., Chesnokova, A., Pellicciotti, F., 2017a. Pond Dynamics and Supraglacial-Englacial Connectivity on Debris-Covered Lirung Glacier, Nepal. Front. Earth Sci. 5. https://doi.org/10.3389/feart.2017.00069

Miles, E.S., Willis, I., Buri, P., Steiner, J.F., Arnold, N.S., Pellicciotti, F., 2018. Surface Pond Energy Absorption Across Four Himalayan Glaciers Accounts for 1/8 of Total Catchment Ice Loss. Geophys. Res. Lett. 0. https://doi.org/10.1029/2018GL079678

Miles, E.S., Willis, I.C., Arnold, N.S., Steiner, J.F., Pellicciotti, F., 2017b. Spatial, seasonal and interannual variability of supraglacial ponds in the Langtang Valley of Nepal, 1999–2013. J. Glaciol. 63, 88–105. https://doi.org/10.1017/jog.2016.120

Mölg, N., Bolch, T., Rastner, P., Strozzi, T., Paul, F., 2018. A consistent glacier inventory for Karakoram and Pamir derived from Landsat data: distribution of debris cover and mapping challenges. Earth Syst. Sci. Data 10, 1807–1827. https://doi.org/10.5194/essd-10-1807-2018

Mölg, N., Bolch, T., Walter, A., Vieli, A., 2019. Unravelling the evolution of Zmuttgletscher and its debris cover since the end of the Little Ice Age. The Cryosphere 13, 1889–1909. https://doi.org/10.5194/tc-13-1889-2019

Nakawo, M., Yabuki, H., Sakai, A., 1999. Characteristics of Khumbu Glacier, Nepal Himalaya: recent change in the debris-covered area. Ann. Glaciol. 28, 118–122. https://doi.org/10.3189/172756499781821788

Nicholson, L., Benn, D.I., 2006. Calculating ice melt beneath a debris layer using meteorological data. J. Glaciol. 52, 463–470. https://doi.org/10.3189/172756506781828584

Nuth, C., Kääb, A., 2011. Co-registration and bias corrections of satellite elevation data sets for quantifying glacier thickness change. The Cryosphere 5, 271. https://doi.org/10.5194/tc-5-271-2011

Østrem, G., 1959. Ice melting under a thin layer of moraine, and the existence of ice cores in moraine ridges. Geogr. Ann. 41, 228–230. https://doi.org/10.1080/20014422.1959.11907953

Paul, F., Barrand, N.E., Baumann, S., Berthier, E., Bolch, T., Casey, K., Frey, H., Joshi, S.P., Konovalov, V., Bris, R.L., Mölg, N., Nosenko, G., Nuth, C., Pope, A., Racoviteanu, A., Rastner, P., Raup, B., Scharrer, K., Steffen, S., Winsvold, S., 2013. On the accuracy of glacier outlines derived from remote-sensing data. Ann. Glaciol. 54, 171–182. https://doi.org/10.3189/2013AoG63A296

Paul, F., Bolch, T., Briggs, K., Kääb, A., McMillan, M., McNabb, R., Nagler, T., Nuth, C., Rastner, P., Strozzi, T., Wuite, J., 2017. Error sources and guidelines for quality assessment of glacier area, elevation change, and velocity products derived from satellite data in the Glaciers_cci project. Remote

Sens. Environ., Earth Observation of Essential Climate Variables 203, 256–275. https://doi.org/10.1016/j.rse.2017.08.038

Paul, F., Kääb, A., Haeberli, W., 2007. Recent glacier changes in the Alps observed by satellite: Consequences for future monitoring strategies. Glob. Planet. Change, Climate Change Impacts on Mountain Glaciers and Permafrost 56, 111–122. https://doi.org/10.1016/j.gloplacha.2006.07.007

Pellicciotti, F., Stephan, C., Miles, E., Herreid, S., Immerzeel, W.W., Bolch, T., 2015. Mass-balance changes of the debris-covered glaciers in the Langtang Himal, Nepal, from 1974 to 1999. J. Glaciol. 61, 373–386. https://doi.org/10.3189/2015JoG13J237

Quincey, D.J., Luckman, A., Benn, D., 2009. Quantification of Everest region glacier velocities between 1992 and 2002, using satellite radar interferometry and feature tracking. J. Glaciol. 55, 596–606. https://doi.org/10.3189/002214309789470987

Quincey, D.J., Richardson, S.D., Luckman, A., Lucas, R.M., Reynolds, J.M., Hambrey, M.J., Glasser, N.F., 2007. Early recognition of glacial lake hazards in the Himalaya using remote sensing datasets. Glob. Planet. Change 56, 137–152. https://doi.org/10.1016/j.gloplacha.2006.07.013

Rabatel, A., Dedieu, J.P., Vincent, C., 2016. Spatio-temporal changes in glacier-wide mass balance quantified by optical remote sensing on 30 glaciers in the French Alps for the period 1983–2014. J. Glaciol. 62, 1153–1166. https://doi.org/10.1017/jog.2016.113

Ragettli, S., Bolch, T., Pellicciotti, F., 2016. Heterogeneous glacier thinning patterns over the last 40 years in Langtang Himal, Nepal. Cryosphere 10, 2075–2097. https://doi.org/10.5194/tc-10-2075-2016

Ragettli, S., Pellicciotti, F., Immerzeel, W.W., Miles, E.S., Petersen, L., Heynen, M., Shea, J.M., Stumm, D., Joshi, S., Shrestha, A., 2015. Unraveling the hydrology of a Himalayan catchment through integration of high resolution in situ data and remote sensing with an advanced simulation model. Adv. Water Resour. 78, 94–111. https://doi.org/10.1016/j.advwatres.2015.01.013

Ravanel, L., Magnin, F., Deline, P., 2017. Impacts of the 2003 and 2015 summer heatwaves on permafrost-affected rock-walls in the Mont Blanc massif. Sci. Total Environ. 609, 132–143. https://doi.org/10.1016/j.scitotenv.2017.07.055

Reid, T.D., Brock, B.W., 2014. Assessing ice-cliff backwasting and its contribution to total ablation of debris-covered Miage glacier, Mont Blanc massif, Italy. J. Glaciol. 60, 3–13. https://doi.org/10.3189/2014JoG13J045

Reid, T.D., Brock, B.W., 2010. An energy-balance model for debris-covered glaciers including heat conduction through the debris layer. J. Glaciol. 56, 903–916. https://doi.org/10.3189/002214310794457218

Reynolds, J.M., 2000. On the formation of supraglacial lakes on debris-covered glaciers. IAHS Publ. 153–164.

Robson, B.A., Nuth, C., Nielsen, P.R., Girod, L., Hendrickx, M., Dahl, S.O., 2018. Spatial Variability in Patterns of Glacier Change across the Manaslu Range, Central Himalaya. Front. Earth Sci. 6. https://doi.org/10.3389/feart.2018.00012

Rowan, A.V., Egholm, D.L., Quincey, D.J., Glasser, N.F., 2015. Modelling the feedbacks between mass balance, ice flow and debris transport to predict the response to climate change of debris-covered glaciers in the Himalaya. Earth Planet. Sci. Lett. 430, 427–438. https://doi.org/10.1016/j.epsl.2015.09.004

Sakai, A., Nakawo, M., Fujita, K., 2002. Distribution Characteristics and Energy Balance of Ice Cliffs on Debris-Covered Glaciers, Nepal Himalaya. Arct. Antarct. Alp. Res. 34, 12–19. https://doi.org/10.2307/1552503

Sakai, A., Nakawo, M., Fujita, K., 1998. Melt rate of ice cliffs on the Lirung Glacier, Nepal Himalayas, 1996. Bull Glacier Res 16, 57–66.

Sakai, A., Takeuchi, N., Fujita, K., Nakawo, M., 2000. Role of supraglacial ponds in the ablation process of a debris-covered glacier in the Nepal Himalayas. IAHS Publ. 119–132.

Salerno, F., Thakuri, S., Tartari, G., Nuimura, T., Sunako, S., Sakai, A., Fujita, K., 2017. Debris-covered glacier anomaly? Morphological factors controlling changes in the mass balance, surface area, terminus position, and snow line altitude of Himalayan glaciers. Earth Planet. Sci. Lett. 471, 19–31. https://doi.org/10.1016/j.epsl.2017.04.039

Scherler, D., Bookhagen, B., Strecker, M.R., 2011. Spatially variable response of Himalayan glaciers to climate change affected by debris cover. Nat. Geosci. 4, 156–159. https://doi.org/10.1038/ngeo1068

Senese, A., Diolaiuti, G., Mihalcea, C., Smiraglia, C., 2012. Energy and Mass Balance of Forni Glacier (Stelvio National Park, Italian Alps) from a Four-Year Meteorological Data Record. Arct. Antarct. Alp. Res. 44, 122–134. https://doi.org/10.1657/1938-4246-44.1.122

Shaw, T.E., Brock, B.W., Fyffe, C.L., Pellicciotti, F., Rutter, N., Diotri, F., 2016. Air temperature distribution and energy-balance modelling of a debris-covered glacier. J. Glaciol. 62, 185–198. https://doi.org/10.1017//jog.2016.31

Sherwood, S., Webb, M.J., Annan, J.D., Armour, K.C., Forster, P.M., Hargreaves, J.C., Hegerl, G., Klein, S.A., Marvel, K.D., Rohling, E.J., Watanabe, M., Andrews, T., Braconnot, P., Bretherton, C.S., Foster, G.L., Hausfather, Z., Heydt, A.S. von der, Knutti, R., Mauritsen, T., Norris, J.R., Proistosescu, C., Rugenstein, M., Schmidt, G.A., Tokarska, K.B., Zelinka, M.D., 2020. An assessment of Earth's climate sensitivity using multiple lines of evidence. Rev. Geophys. n/a, e2019RG000678. https://doi.org/10.1029/2019RG000678

Silverio, W., Jaquet, J.-M., 2005. Glacial cover mapping (1987–1996) of the Cordillera Blanca (Peru) using satellite imagery. Remote Sens. Environ. 95, 342–350. https://doi.org/10.1016/j.rse.2004.12.012

Smiraglia, C., Diolaiuti, G., Casati, D., Kirkbride, M.P., 2000. Recent areal and altimetric variations of Miage Glacier (Monte Bianco massif, Italian Alps). IAHS Publ. 264 227–233.

Steiner, J.F., Buri, P., Miles, E.S., Ragettli, S., Pellicciotti, F., 2019. Supraglacial ice cliffs and ponds on debris-covered glaciers: spatio-temporal distribution and characteristics. J. Glaciol. 1–16. https://doi.org/10.1017/jog.2019.40

Thompson, S., Benn, D.I., Mertes, J., Luckman, A., 2016. Stagnation and mass loss on a Himalayan debris-covered glacier: processes, patterns and rates. J. Glaciol. 62, 467–485. https://doi.org/10.1017/jog.2016.37

Thomson, M.H., Kirkbride, M.P., Brock, B.W., 2000. Twentieth century surface elevation change of the Miage Glacier, Italian Alps. IAHS Publ. 264 219–226.

Tinti, S., Maramai, A., Cerutti, A.V., 1999. The Miage Glacier in the Valley of Aosta (Western Alps, Italy) and the extraordinary detachment which occurred on August 9, 1996. Phys. Chem. Earth Part Solid Earth Geod. 24, 157–161. https://doi.org/10.1016/S1464-1895(99)00012-5

Tonkin, T.N., Midgley, N.G., 2016. Ground-Control Networks for Image Based Surface Reconstruction: An Investigation of Optimum Survey Designs Using UAV Derived Imagery and Structure-from-Motion Photogrammetry. Remote Sens. 8, 786. https://doi.org/10.3390/rs8090786

Vincent, C., Fischer, A., Mayer, C., Bauder, A., Galos, S.P., Funk, M., Thibert, E., Six, D., Braun, L., Huss, M., 2017. Common climatic signal from glaciers in the European Alps over the last 50 years. Geophys. Res. Lett. 44, 1376–1383. https://doi.org/10.1002/2016GL072094

Vincent, C., Soruco, A., Six, D., Meur, E.L., 2009. Glacier thickening and decay analysis from 50 years of glaciological observations performed on Glacier d'Argentière, Mont Blanc area, France. Ann. Glaciol. 50, 73–79. https://doi.org/10.3189/172756409787769500

Vincent, C., Wagnon, P., Shea, J.M., Immerzeel, W.W., Kraaijenbrink, P., Shrestha, D., Soruco, A., Arnaud, Y., Brun, F., Berthier, E., Sherpa, S.F., 2016. Reduced melt on debris-covered glaciers: investigations from Changri Nup Glacier, Nepal. The Cryosphere 10, 1845–1858. https://doi.org/10.5194/tc-10-1845-2016

Watson, C.S., Quincey, D.J., Carrivick, J.L., Smith, M.W., 2017a. Ice cliff dynamics in the Everest region of the Central Himalaya. Geomorphology 278, 238–251. https://doi.org/10.1016/j.geomorph.2016.11.017

Watson, C.S., Quincey, D.J., Carrivick, J.L., Smith, M.W., Rowan, A.V., Richardson, R., 2018. Heterogeneous water storage and thermal regime of supraglacial ponds on debris-covered glaciers. Earth Surf. Process. Landf. 43, 229–241. https://doi.org/10.1002/esp.4236

Watson, C.S., Quincey, D.J., Smith, M.W., Carrivick, J.L., Rowan, A.V., James, M.R., 2017b. Quantifying ice cliff evolution with multi-temporal point clouds on the debris-covered Khumbu Glacier, Nepal. J. Glaciol. 63, 823–837. https://doi.org/10.1017/jog.2017.47

Westoby, M.J., Dunning, S.A., Woodward, J., Hein, A.S., Marrero, S.M., Winter, K., Sugden, D.E., 2016. Interannual surface evolution of an Antarctic blue-ice moraine using multi-temporal DEMs. Earth Surf. Dyn. 4, 515–529. https://doi.org/10.5194/esurf-4-515-2016

Westoby, M.J., Rounce, D.R., Shaw, T.E., Fyffe, C.L., Moore, P.L., Stewart, R.L., Brock, B.W., 2020. Geomorphological evolution of a debris-covered glacier surface. Earth Surf. Process. Landf. n/a. https://doi.org/10.1002/esp.4973

Zekollari, H., Huss, M., Farinotti, D., 2020. On the Imbalance and Response Time of Glaciers in the European Alps. Geophys. Res. Lett. 47, e2019GL085578. https://doi.org/10.1029/2019GL085578

Zemp, M., Frey, H., Gärtner-Roer, I., Nussbaumer, S.U., Hoelzle, M., Paul, F., Haeberli, W., Denzinger, F., Ahlstrøm, A.P., Anderson, B., Bajracharya, S., Baroni, C., Braun, L.N., Cáceres, B.E., Casassa, G., Cobos, G., Dávila, L.R., Delgado Granados, H., Demuth, M.N., Espizua, L., Fischer, A., Fujita, K., Gadek, B., Ghazanfar, A., Hagen, J.O., Holmlund, P., Karimi, N., Li, Z., Pelto, M., Pitte, P., Popovnin, V.V., Portocarrero, C.A., Prinz, R., Sangewar, C.V., Severskiy, I., Sigurðsson, O., Soruco, A., Usubaliev, R., Vincent, C., 2015. Historically unprecedented global glacier decline in the early 21st century. J. Glaciol. 61, 745–762. https://doi.org/10.3189/2015JoG15J017